

# Dual-structure-breaking electrolyte enables practical cadmium-metal battery

Received: 23 July 2024

Accepted: 3 June 2025

Published online: 01 July 2025

Yang-Feng Cui<sup>1,4</sup>, Hao-Bin Song<sup>1,4</sup>, Jing-Jing Yao<sup>1</sup>, Qi Hao<sup>2</sup>, Xue-Liang Li<sup>1</sup>, Yi-Fan Li<sup>1</sup>, Bin-Bin Guo<sup>1</sup>, Yun-Hai Zhu<sup>3</sup> & Hui Ying Yang<sup>1</sup>✉

High-energy aqueous metal batteries are promising candidates for the next-generation energy storage systems but face critical challenges of dendrite and corrosion in metal negative electrodes. To address these issues, we report an aqueous cadmium-metal battery employing a fast-kinetics structure-breaking electrolyte composed of  $\text{CdCl}_2$  and  $\text{NH}_4\text{Cl}$ . The addition of  $\text{NH}_4\text{Cl}$  induces the formation of dual structure breakers,  $\text{NH}_4^+$  and tetrachlorocomplex ( $[\text{CdCl}_4]^{2-}$ ), which facilitate fast charge transfer kinetics in aqueous cadmium-metal batteries and endow dendrite-free/corrosion-resistant capabilities to Cd negative electrodes. This tailored electrolyte realizes a convincing Coulombic efficiency (99.93%) for Cd plating/stripping behavior at a high Cd utilization of 55%, making it suitable for practical applications. Moreover, the fast-kinetics aqueous cadmium-metal batteries exhibit remarkable compatibility with diverse types of positive electrodes, including conversion-, coordination-, intercalation- and capacitance-type, offering enhanced rate performance and durable rechargeable stability. These results establish a robust and scalable aqueous battery design for sustainable energy storage systems.

The transition from carbon-rich fossil fuels to environmentally friendly renewable energy sources to achieve decarbonization has become a fundamental goal across academia, industry, and government<sup>1</sup>. However, the increasing reliance on renewable but intermittent energy sources—such as solar, wind, and tidal power—necessitates the development of cost-effective, safe, and durable energy storage solutions for large-scale electricity storage<sup>2</sup>. Although lithium-ion batteries have successfully dominated the market for high specific energy applications, they may not be the optimal choice for all scenarios, particularly for grid-scale energy storage, due to their reliance on flammable organic electrolytes and scarce electrode materials<sup>3</sup>. In contrast, aqueous metal batteries have emerged as promising candidates in various energy storage contexts, offering high power density, fast-charging capability, minimized safety risks and lower manufacturing costs<sup>4</sup>.

However, the key challenge lies in lack of reliable aqueous energy storage systems to support the decarbonization of renewable electricity generation. This explains why century-old lead-acid batteries,

despite their low specific energy (30–50 Wh kg<sup>-1</sup>), remain essential for grid-scale energy storage, portable electronics and electric vehicles<sup>5,6</sup>. In recent years, rechargeable aqueous zinc-metal batteries (AZBs) have been considered promising candidates for multi-scenario storage applications<sup>7,8</sup>. The metallic zinc (Zn) is one of the few metal negative electrode capable of reversible plating/stripping behavior in aqueous media while offering a suitable redox potential (−0.76 V vs. standard hydrogen electrode, SHE) and high specific capacity (820 mAh g<sup>-1</sup>). AZBs fitted with manganese (Mn)-based, vanadium (V)-based, and organic positive electrodes are attractive for their high theoretical specific energy (60–250 Wh kg<sup>-1</sup>)<sup>9</sup>. However, the fatal issues of cell shorting by dendrites and passivation due to corrosion have hindered the deployment of this technology<sup>10,11</sup>.

Motivated by this background, several emerging metal negative electrodes are being investigated as potential alternatives to Zn negative electrodes, such as iron (Fe)<sup>12–15</sup>, indium (In)<sup>16–18</sup>, nickel (Ni)<sup>19</sup>, tin (Sn)<sup>20–23</sup>, copper (Cu)<sup>24,25</sup>, and bismuth (Bi)<sup>26</sup>. While these metal

<sup>1</sup>Pillar of Engineering Product Development, Singapore University of Technology and Design, Singapore, Singapore. <sup>2</sup>School of Materials Science and Engineering, Zhejiang University, Hangzhou, China. <sup>3</sup>State Key Laboratory of New Textile Materials and Advanced Processing, Wuhan Textile University, Wuhan, China. <sup>4</sup>These authors contributed equally: Yang-Feng Cui, Hao-Bin Song. ✉e-mail: [yanghuiying@sutd.edu.sg](mailto:yanghuiying@sutd.edu.sg)

negative electrodes exhibit impressive electrochemical properties, they still face varying degrees of challenges for next-generation energy storage applications (Fig. 1a). For instance, Fe negative electrodes suffer from passivation reactions that hinder ionic transport<sup>27</sup>. In is a rare and noble metal, making it unsuitable for large-scale energy storage<sup>28</sup>. The plating/stripping behavior of Ni negative electrode exhibits sluggish kinetics, resulting in high potential polarization<sup>19,29</sup>. The redox potentials of the  $\text{Cu}^{2+}/\text{Cu}$  (+0.34 V vs. SHE) and  $\text{Bi}^{3+}/\text{Bi}$  (+0.32 V vs. SHE) couples are too high for practical use in batteries<sup>24,30</sup>. In contrast, acidic Sn-metal batteries paired with acidic positive electrodes show greater promise, whereas preventing  $\text{Sn}^{2+}$  shuttle and the subsequent redox reactions of  $\text{Sn}^{4+}/\text{Sn}^{2+}$  at the positive electrode surface is a prerequisite for ensuring the normal cycling of the battery<sup>31</sup>. To address these challenges, recently, Wu's group proposed a competitive aqueous cadmium-metal battery (ACB) utilizing a  $1\text{ mol L}^{-1}$   $\text{CdCl}_2$  electrolyte<sup>32</sup>. Herein, the metallic cadmium (Cd) negative electrode not only possesses the dendrite-resistant and corrosion-resistant capabilities but also exhibits a high specific capacity ( $477\text{ mAh g}^{-1}$ ) and a suitable redox potential ( $-0.40\text{ V}$  vs. SHE), as shown in Fig. 1a. This gives Cd negative electrode several advantages over other metal anodes, including the Zn negative electrode (Fig. 1a, b). While the study by Wu et al primarily aims to advance the understanding of Cd plating chemistry, it also highlights the practical significance of developing ACBs<sup>32</sup>. Furthermore, Cd is inherently present in Zn ores, such as  $\text{Zn}(\text{Cd})\text{S}$ , with approximately 90–98% of global Cd resources found in these deposits<sup>33</sup>. As a result, Cd extraction is an inevitable by-product of Zn mining and refining<sup>34</sup>. Advancing ACB technology not only offers a meaningful application for this by-product but also complements the ongoing development of Zn-based energy storage systems.

In this work, we introduce the ACB operating with a fast-kinetics structure breaking electrolyte (SBE) composed of  $\text{CdCl}_2 + \text{NH}_4\text{Cl}$ . Unlike classical water-in-salt electrolytes<sup>35–39</sup>, which reduce  $\text{H}_2\text{O}$  activity by increasing salt concentration but compromise charge transfer kinetics due to their high viscosity and low ionic conductivity<sup>40</sup>, the SBE achieves fast-kinetics advantage by leveraging the concept of structure breaker. The structure breaking is a strategy that introduces/forms specific structure breakers, e.g.,  $\text{K}^+$ ,  $\text{NH}_4^+$ ,  $\text{Cl}^-$ , and  $[\text{AuCl}_4]^-$  with large sizes and low charge densities, which form loosely bound solvation shells, enhancing diffusion and lowering viscosity of solutions<sup>41–43</sup>. Our proposed SBE inherits these features. The inclusion of concentrated  $\text{NH}_4\text{Cl}$  promotes the formation of dual structure breakers,  $\text{NH}_4^+$  and tetrachloro complex ( $[\text{CdCl}_4]^{2-}$ ), which disrupt the ordered  $\text{H}_2\text{O}$  molecule structure, reduce electrolyte viscosity, and enhance exchange current of ACBs. Therefore, the SBE facilitates the fast kinetics in ACBs and endows dendrite-free and corrosion-resistant capabilities in Cd negative electrodes. As a result, the tailored SBE enables convincing Coulombic efficiency (CE) of 99.93% and the aging CE of 99.34% for Cd plating/stripping behaviors at a high negative electrode utilization (NEU) of 55% ( $5\text{ mAh cm}^{-2}$ ). This practical performance makes numerous high-energy and durable aqueous batteries based on Cd negative electrode and SBE possible, including but not limited to  $\text{Cd}||\text{I}_2$  cells,  $\text{Cd}||\text{MnO}_2$  cells,  $\text{Cd}||\text{V}_2\text{O}_5$  cells,  $\text{Cd}||\text{organic}$  cells,  $\text{Cd}||\text{air}$  cells, and Cd-ion hybrid capacitors (Fig. 1c, d). Their diversity and universality are demonstrated through the use of four representative types of positive electrodes, intercalation-type  $\text{V}_2\text{O}_5$ , capacitance-type active carbon (AC), coordination-type organic polyaniline (PANI), and conversion-type  $\text{CdI}_2$ . Overall, our work suggests a practical ACB with the potential to support robust energy storage applications.

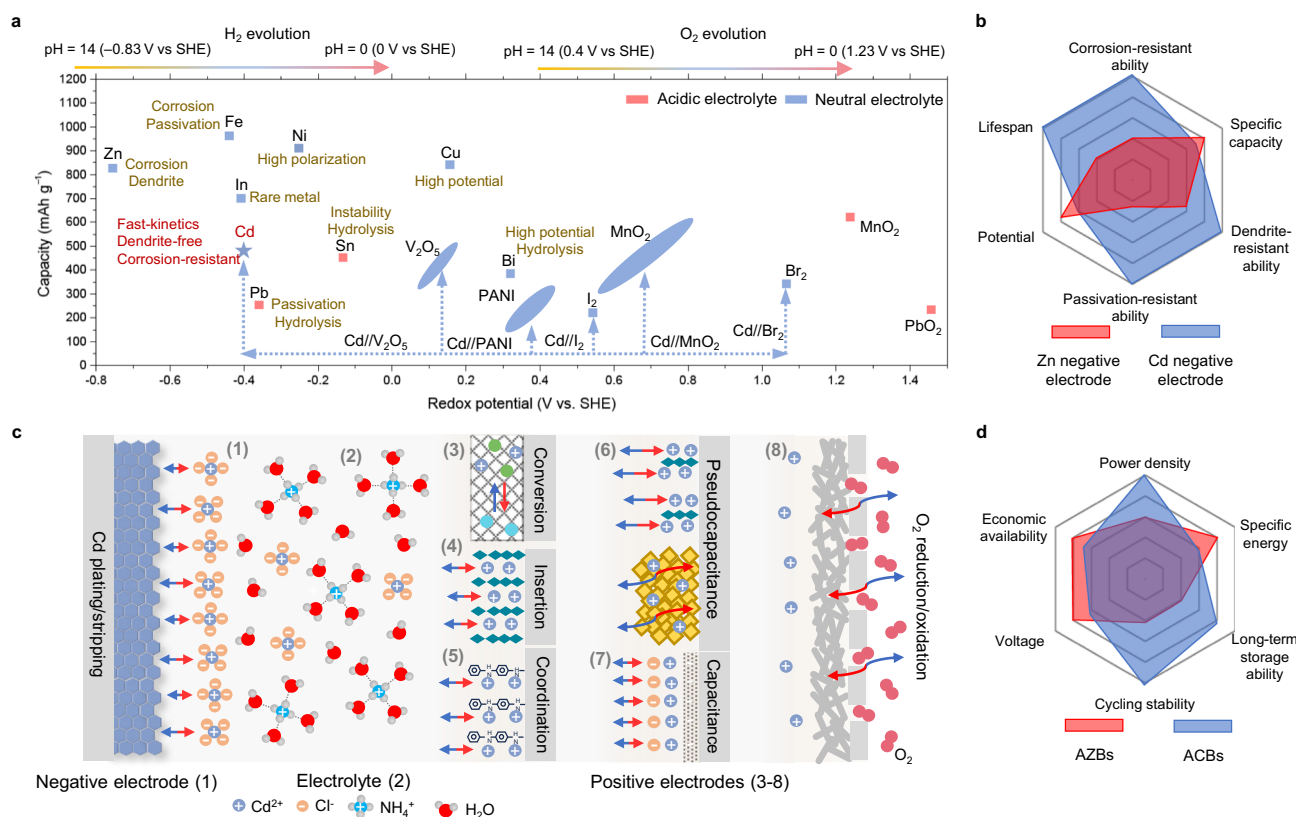


**Fig. 1 | ACBs for energy storage applications.** **a** Schematic of redox potentials, specific capacities, and characteristics of different electrodes in aqueous electrolytes. **b** Advantages of Cd negative electrode compared to Zn negative electrode. **c** Schematic diagram of the proposed ACBs featuring a Cd negative electrode and

electrolyte, paired various types of positive electrodes, including conversion-, insertion-, coordination-, capacitance-type positive electrodes. **d** Advantages of ACBs compared to AZBs.

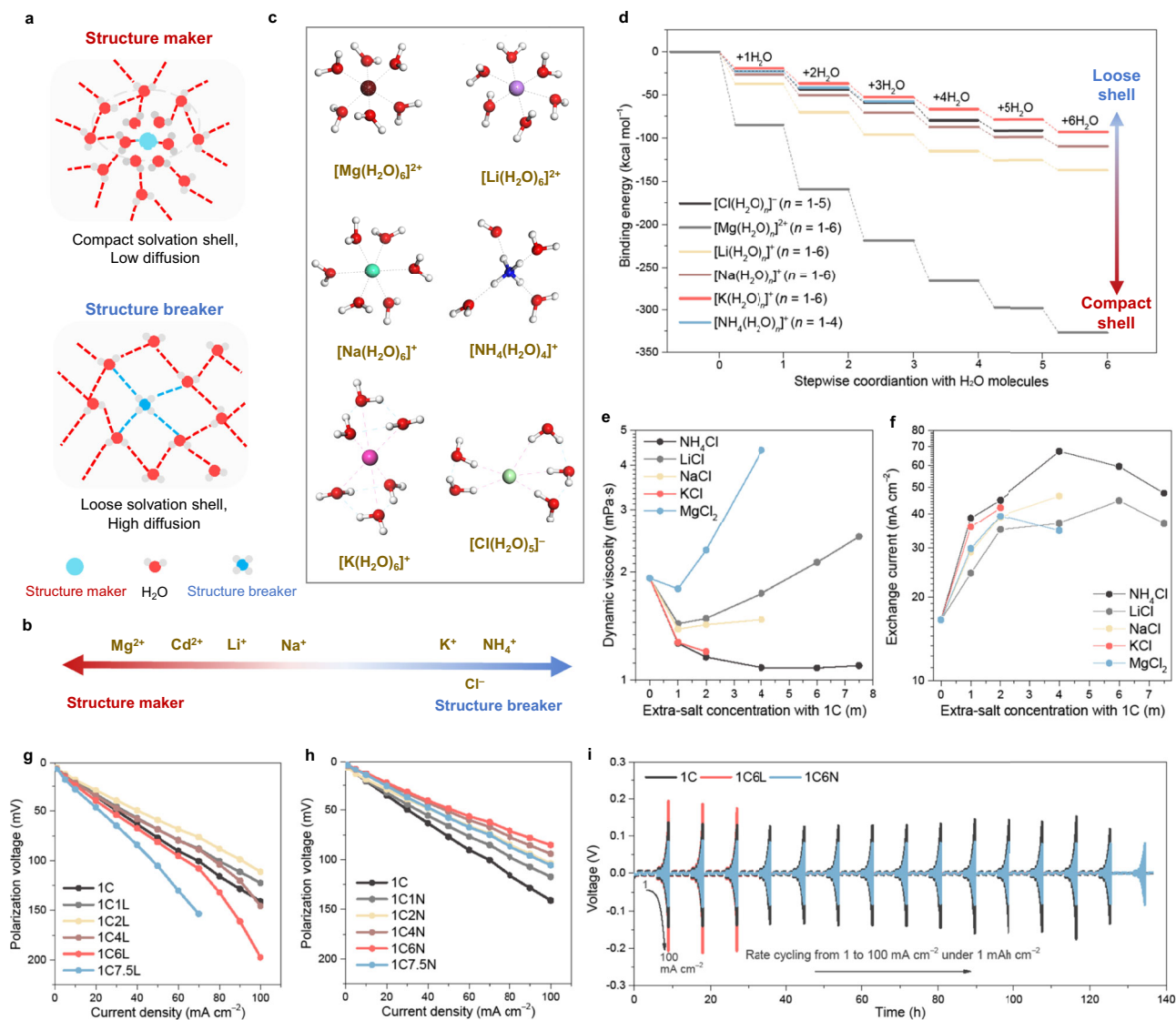


**Fig. 2 | Fundamentals of structure maker and structure breaker.** **a** Schematic of compact solvation shell enabled by structure maker and loose solvation shell enabled by structure breaker. **b** Structure making and breaking ability for different ions. **c, d** DFT for primary solvation shells (**c**) and binding energies with stepwise coordination of H<sub>2</sub>O molecules (**d**). The H, O, Mg, Li, Na, N, K, and Cl atoms are represented by white, red, brown, purple, turquoise, blue, pink, and light green spheres, respectively in (**c**). **e, f** Dynamic viscosity (**e**) and exchange current (**f**) of 1C

electrolyte without/with extra chlorides with increased concentrations. See Supplementary Figs. 8–13 for details on exchange current measurements. **g, h** Polarization voltage of Cd||Cd symmetric cells at different current densities in CdCl<sub>2</sub> + LiCl system (**g**) and CdCl<sub>2</sub> + NH<sub>4</sub>Cl system (**h**). **i** Corresponding current density-varied Cd plating/stripping performance of Cd||Cd symmetric cells in 1C, 1C6L, and 1C6N electrolytes (derived from Supplementary Figs. 18–23). An average testing temperature of 25 ± 2 °C was maintained in (**f–i**).

## Results

### Guidelines for structure maker and structure breaker

Before beginning the discussion in this work, we first introduce two microscopic structures in aqueous media: one associated with structure maker and the other with structure breaker<sup>43</sup>. Small ions of high charge density bind strongly to H<sub>2</sub>O molecules (structure makers), thus making a more orderly and compact arrangement of H<sub>2</sub>O molecules (top of Fig. 2a), whereas large ions of low charge density interact weakly with water molecules (structure breakers), which disrupted the hydrogen bond network and reduced structural integrity compared to bulk H<sub>2</sub>O molecules (bottom of Fig. 2a)<sup>44</sup>. Based on this characteristic, common ions can be classified as either structure makers ( $Mg^{2+}$ ,  $Cd^{2+}$ ,  $Li^+$ , and  $Na^+$ ) or structure breakers ( $Cl^-$ ,  $K^+$ , and  $NH_4^+$ ), as shown in Fig. 2b, Supplementary Fig. 1, and Supplementary Note 1.

Density functional theory (DFT) simulations revealed that the strong ion-dipole interactions between structure-breaking  $Li^+$ ,  $Na^+$ , or  $Mg^{2+}$  and H<sub>2</sub>O molecules resulted in compact octahedral solvation

shells with six H<sub>2</sub>O molecules (Fig. 2c), characterized by strong binding energies of 137.704, 110.028, and 326.243 kcal mol<sup>-1</sup> for  $[Li(H_2O)_6]^+$ ,  $[Na(H_2O)_6]^+$  and  $[Mg(H_2O)_6]^{2+}$ , respectively (Fig. 2d). However, distinct solvation shells were observed in the structure breakers (Fig. 2c). Specifically,  $NH_4^+$  formed a weakly bound tetrahedral coordination shell,  $[NH_4(H_2O)_4]^+$ , through hydrogen bonding, characterized by the lowest binding energy of 70.951 kcal mol<sup>-1</sup> (Fig. 2d); on the other hand, the  $K^+$  and  $Cl^-$  formed looser solvation shells due to weaker ion-dipole interactions, as evidenced by their low binding energies of 93.150 and 91.496 kcal mol<sup>-1</sup> for  $[K(H_2O)_6]^+$  and  $[Cl(H_2O)_5]^-$ , respectively (Fig. 2c, d). The detailed stepwise DFT simulations of loose/compact coordination environments are detailed in the Supplementary Figs. 2–7, Supplementary Tables 1–14, and Supplementary Note 2.

The structure-making or structure-breaking behavior of solutes in aqueous solutions can be inferred from their effects on viscosity and exchange dynamics of H<sub>2</sub>O molecules. Structure breakers typically reduce viscosity and lower the activation energy required for H<sub>2</sub>O

exchange, facilitating a more dynamic aqueous environment; in contrast, structure makers increase viscosity and stabilize the hydrogen bonding network, raising the activation energy for H<sub>2</sub>O exchange. Furthermore, changes in viscosity directly influence the mass transfer and diffusion properties of the electrolytes. Leveraging these trends, we subsequently started with the baseline electrolyte of 1 m CdCl<sub>2</sub> (referred to as 1C) to investigate how the addition of extra structure breakers/makers influences its viscosity and charge transfer kinetics of electrolytes. Note that, due to solubility limitations, not all additional chlorides can achieve a concentration of 7.5 m in the 1C electrolyte, with the exception of LiCl and NH<sub>4</sub>Cl. Clearly, the 1C electrolyte markedly raised the dynamic viscosity of the pure water from 1.00 mPa·s to 1.92 mPa·s, due to the nature of structure maker of Cd<sup>2+</sup> with high charge density (Fig. 2e)<sup>43</sup>. However, besides the initial decrease in the viscosity, the introduction of LiCl, NaCl and MgCl<sub>2</sub> gradually increased the viscosity with increased concentrations, whose trend closely correlated with the hydration capacities of these structure makers (Mg<sup>2+</sup> > Li<sup>+</sup> > Na<sup>+</sup>). We attributed this initial decrease in viscosity to the possible competing roles between structure breaker (Cl<sup>−</sup>) and structure maker (Li<sup>+</sup>, Na<sup>+</sup>, or Mg<sup>2+</sup>), as discussed Supplementary Note 3. However, the gradually increased concentration of structure makers strengthened their interaction with H<sub>2</sub>O molecules, resulting in a subsequent rise in viscosity as concentration continues to increase. Interestingly, introducing structure-breaking NH<sub>4</sub>Cl and KCl in 1C electrolyte resulted in a rapid decrease in electrolyte viscosity (Fig. 2e). Notably, the viscosities of the electrolytes containing 1 m CdCl<sub>2</sub> + 1 m NH<sub>4</sub>Cl (1C1N), 1 m CdCl<sub>2</sub> + 2 m NH<sub>4</sub>Cl (1C2N), 1 m CdCl<sub>2</sub> + 4 m NH<sub>4</sub>Cl (1C4N), 1 m CdCl<sub>2</sub> + 6 m NH<sub>4</sub>Cl (1C6N), and 1 m CdCl<sub>2</sub> + 7.5 m NH<sub>4</sub>Cl (1C7.5N) are only slightly above that of pure water, with values of 1.265, 1.156, 1.081, 1.079, and 1.095 mPa·s, respectively.

We subsequently quantified the charge-transfer kinetics in structure-breaking/structure-making systems by measuring the exchange currents of Cd||Cd symmetric cells, as summarized in Fig. 2f and derived from Supplementary Figs. 8–13. Since we confirmed through limiting currents that exchange currents were conducted under non transport limited conditions (Supplementary Fig. 14), the obtained exchange currents can directly reflect the intrinsic charge-transfer kinetics of ion transport, solvation/desolvation, and plating/stripping processes<sup>45</sup>. It was observed that the structure breaker of NH<sub>4</sub>Cl enables the fastest charge transfer kinetics compared to other salts, reflecting in the high exchange currents of 66.7 mA cm<sup>−2</sup> and 58.9 mA cm<sup>−2</sup> in 1C4N and 1C6N electrolytes, respectively (Fig. 2f). In addition, we also observed an improvement in the charge-transfer kinetics even as the electrolyte viscosity increased while introducing structure makers, which may be related to Cl<sup>−</sup> acting as a structure breaker and its coordination with Cd<sup>2+</sup> accelerated charge transfer process (Supplementary Figs. 15–17, Supplementary Tables 15–28, and Supplementary Note 4).

Since the exchange current reflects charge-transfer kinetics under non-mass-transport-limited conditions, whereas charge transfer during practical cell operation is a continuous process that may involve ion transport limitations, we further analyzed the polarization behavior of Cd||Cd symmetric cells to assess steady-state charge-transfer kinetics (Fig. 2g, h and Supplementary Figs. 18–23). Supporting LiCl and NH<sub>4</sub>Cl, sharing the same valence and parallel concentration but opposite structure-making/breaking properties, were selected for comparison. Interestingly, although CdCl<sub>2</sub> + LiCl system, including 1C + 1 m LiCl (1C1L), 1C + 2 m LiCl (1C2L), 1C + 4 m LiCl (1C4L), 1C + 6 m LiCl (1C6L), and 1C + 7.5 m LiCl (1C7.5L), showed relatively high exchange currents (Fig. 2f), 1C6L and 1C7.5L systems exhibited much higher polarization at higher current densities than 1C system, indicating inferior charge-transfer kinetics during sustained Cd plating/stripping (Fig. 2g). In contrast, NH<sub>4</sub>Cl greatly reduced cell polarization (Fig. 2h), with 1C6N system showing only 85.2 mV at 100 mA cm<sup>−2</sup> vs. 141.2 mV for 1C system. Current density-varied Cd plating/stripping tests further

confirmed these trends: 1C6N system maintained low polarization and stable plating/stripping over 1–100 mA cm<sup>−2</sup> and back, while 1C6L system failed after third sequence of Cd plating/stripping at 100 mA cm<sup>−2</sup> (Fig. 2i). Notably, although the ionic conductivity of the CdCl<sub>2</sub> + LiCl system increased with the increased concentration of LiCl (Supplementary Fig. 24), its current density-varied plating/stripping capability gradually deteriorated (Supplementary Figs. 18–23), highlighting that extra structure-making Li<sup>+</sup> contributed to the high conductivity but restricted the Cd<sup>2+</sup> charge transfer process; conversely, in CdCl<sub>2</sub> + NH<sub>4</sub>Cl system, both conductivity and rate stability improved with increasing NH<sub>4</sub>Cl, confirming that structure-breaking environments promote fast kinetics (Supplementary Figs. 18–24). Finally, we systematically examined current density-varied charge-transfer kinetics across various structure-breaking and/or structure-making systems, reaffirming the critical role of structure breakers (Supplementary Fig. 25 and Supplementary Note 5). Overall, building on the improvements in electrolyte viscosity and charge-transfer kinetics achieved with the structure-breaking NH<sub>4</sub>Cl, we focused our subsequent investigation on how structure breaker-induced SBE influences the electrochemistry of ACBs.

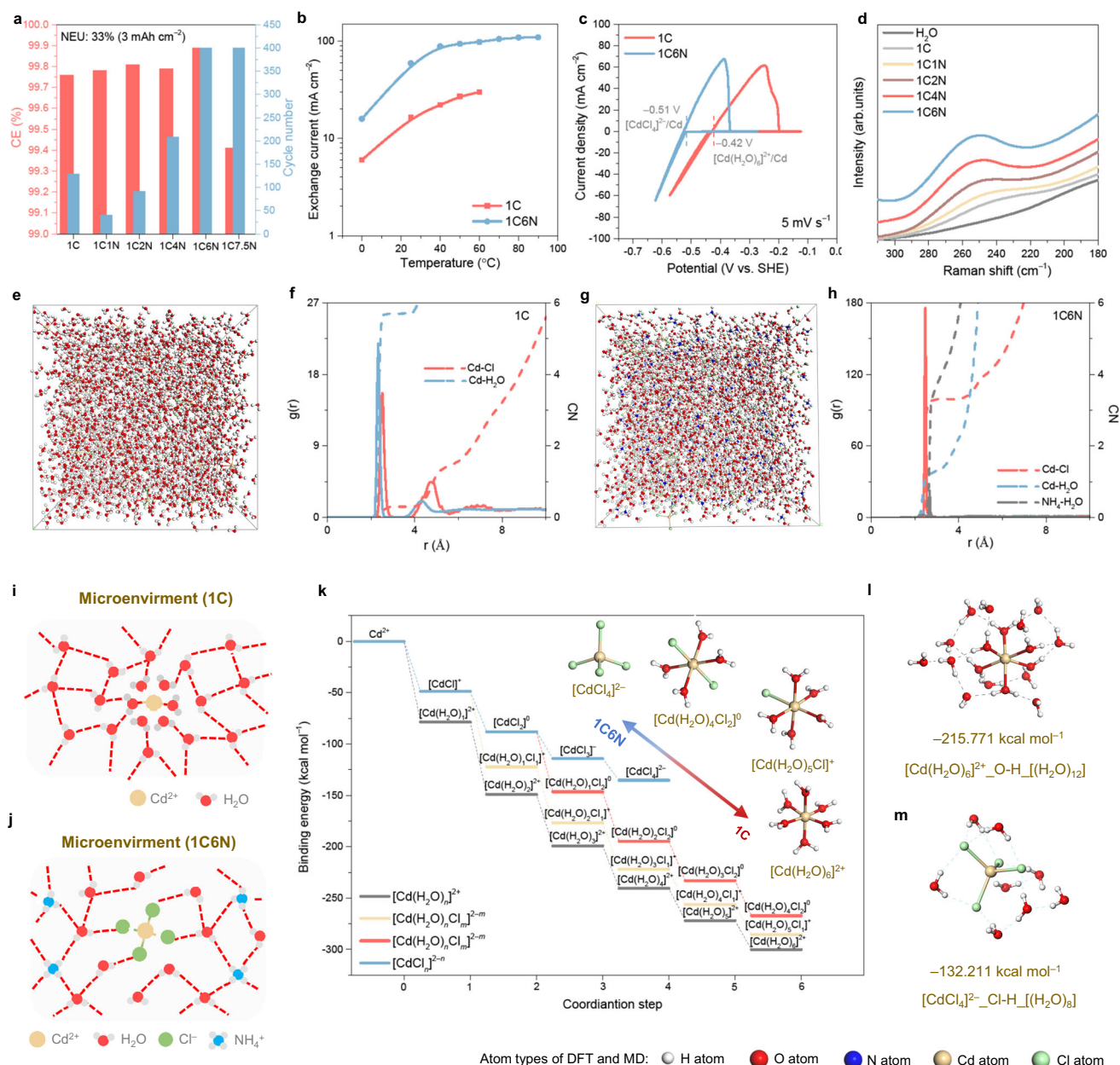
### Fundamentals of SBE

Figure 3a summarized the CEs of Cd||Cu cells in different electrolytes at a substantial NEU of 33% (3 mAh cm<sup>−2</sup>), highlighting the high average CE of 99.89% over 400 cycles in the 1C6N electrolyte (Supplementary Figs. 26, 27). Therefore, the addition of 6 m NH<sub>4</sub>Cl significantly enhanced the performance of the Cd negative electrode, establishing the 1C6N electrolyte as the optimal choice for the subsequent research. This electrolyte demonstrated ultrafast charge-transfer kinetics across a wide temperature range, evidenced by a high exchange current of 15.89 mA cm<sup>−2</sup> at 0 ± 0.5 °C and a limiting exchange current of 109.07 mA cm<sup>−2</sup> at 90 ± 0.5 °C—both markedly superior to those of the 1C electrolyte (Fig. 3b, derived from Supplementary Figs. 28 and 29).

The cyclic voltammetry (CV) profiles showed that the SBE enabled a lower redox potential for the Cd<sup>2+</sup>/Cd couple compared to the 1C electrolyte, shifting from −0.42 V vs. SHE in the 1C electrolyte to −0.51 V vs. SHE in the 1C6N electrolyte (Fig. 3c). The slight shift in the potential in the 1C electrolyte from the standard Cd<sup>2+</sup>/Cd potential (0.40 V vs. SHE) is likely due to minor differences between actual and ideal testing conditions. In contrast, the significant negative shift to −0.51 V vs. SHE of Cd<sup>2+</sup>/Cd in the 1C6N electrolyte is primarily attributed to the involvement of Cl<sup>−</sup> ligands in the redox reaction of the [CdCl<sub>4</sub>]<sup>2−</sup>/Cd couple, as validated by the Nernst equation derivation in Supplementary Note 6. It is similar to the classical Cl<sup>−</sup> coordination in the concentrated ZnCl<sub>2</sub> electrolytes, where the transition from [Zn(H<sub>2</sub>O)<sub>6</sub>]<sup>2+</sup> to [ZnCl<sub>4</sub>]<sup>2−</sup> with increasing chloride concentration effectively reduces H<sub>2</sub>O activity by replacing the aqua ligands of Zn<sup>2+</sup> with the strong Lewis base Cl<sup>−</sup><sup>35,36,46–48</sup>. This key transition accelerates charge diffusion, lowers desolvation barrier, and facilitates uniform Zn plating/stripping behavior while suppressing hydrogen evolution reaction (HER)<sup>39,49–51</sup>. Furthermore, the formation of [CdCl<sub>4</sub>]<sup>2−</sup> was further confirmed by the Raman peak around 260 cm<sup>−1</sup><sup>52,53</sup>, which intensified with increasing NH<sub>4</sub>Cl concentration (Fig. 3d). It is worth noting that although the potential hydrated chloride complex, [Cd(H<sub>2</sub>O)<sub>y</sub>Cl<sub>x</sub>]<sup>2−x</sup>, could showed Cd–Cl stretching at similar Raman frequencies<sup>54</sup>, we inferred that the Cd<sup>2+</sup> predominantly existed in the form of [CdCl<sub>4</sub>]<sup>2−</sup> species due to the well-matched practical and theoretical potentials (Supplementary Note 6).

To visualize this conclusion, molecular dynamics (MD) simulations were conducted to analyze the solvation shells of the 1C and 1C6N electrolytes, as shown in the MD snapshots for 1C electrolyte (Fig. 3e) and 1C6N electrolyte (Fig. 3g). The radial distribution function (RDF) profile of 1C electrolyte, used as a baseline, showed a primary Cd–O peak at −2.3 Å with a coordination number (CN) of ~5.7, and a





**Fig. 3 | Proposed dual-structure-breaking electrolyte. a** Average CE and cycle number in different electrolytes at 2 mA cm<sup>-2</sup> and 3 mA h cm<sup>-2</sup> with a NEU of 33%. **b** Exchange current in 1C and 1C6N electrolytes at different testing temperatures (derived from Supplementary Figs. 28, 29). **c** Three-electrode CV profiles of Cd plating/stripping behavior in 1C and 1C6N electrolytes at a scan rate of 5 mV s<sup>-1</sup>, measured at an average testing temperature of 25 ± 2 °C. **d** Raman spectra of different electrolytes. **e, f** Snapshot of MD simulation (**e**) and RDF and CN (**f**) of 1C

electrolyte. **g, h** Snapshot of MD simulation (**g**) and RDF and CN (**h**) of 1C6N electrolyte. **i, j** Schematic microenvironment of 1C electrolyte (**i**) and 1C6N electrolyte (**j**). **k** DFT simulations for stepwise-coordination solvation shells of [Cd(H<sub>2</sub>O)<sub>6</sub>]<sup>2+</sup>, [Cd(H<sub>2</sub>O)<sub>5</sub>Cl]<sup>+</sup>, [Cd(H<sub>2</sub>O)<sub>4</sub>Cl<sub>2</sub>]<sup>0</sup> and [CdCl<sub>4</sub>]<sup>2-</sup>. **l, m** DFT simulations for inner [Cd(H<sub>2</sub>O)<sub>6</sub>]<sup>2+</sup> with outer H<sub>2</sub>O molecules (**l**) and inner [CdCl<sub>4</sub>]<sup>2-</sup> with outer H<sub>2</sub>O molecules (**m**).

secondary Cd–Cl peak at -2.5 Å with a CN of -0.3 (Fig. 3f), indicating Cd<sup>2+</sup> primarily existed as [Cd(H<sub>2</sub>O)<sub>6</sub>]<sup>2+</sup> species, with minor [Cd(H<sub>2</sub>O)<sub>5</sub>Cl]<sup>+</sup> species (Supplementary Fig. 30). Introducing 6 m NH<sub>4</sub>Cl shifted this coordination environment: the RDF profile showed a main Cd–Cl peak at -2.5 Å (CN: -3.3) and a weaker Cd–O peak at -2.3 Å (CN: -1.2) (Fig. 3h). It confirmed that NH<sub>4</sub>Cl provided extra Cl<sup>-</sup> as Lewis base, transforming [Cd(H<sub>2</sub>O)<sub>6</sub>]<sup>2+</sup> species into primary [CdCl<sub>4</sub>]<sup>2-</sup> species, with minor [Cd(H<sub>2</sub>O)<sub>4</sub>Cl<sub>2</sub>]<sup>0</sup> and [Cd(H<sub>2</sub>O)<sub>5</sub>Cl]<sup>+</sup> species (Supplementary Fig. 30). In addition, NH<sub>4</sub><sup>+</sup> primarily formed a tetra-coordinated [NH<sub>4</sub>(H<sub>2</sub>O)<sub>4</sub>]<sup>+</sup> complex via hydrogen bonding, shown by a peak at -2.7 Å with CN values between 3.3 and 4.0 (Fig. 3h). The hydrated NH<sub>4</sub><sup>+</sup> species were reflected in the Fourier transform infrared spectroscopy

(FTIR; Supplementary Fig. 31), which participated in the formation of the new hydrogen bonding network and decreased hydrogen bonding interactions among H<sub>2</sub>O molecules, as further confirmed by the nuclear magnetic resonance (NMR; Supplementary Fig. 32) and high-frequency Raman (Supplementary Figs. 33, 34). We thus identified two primary electrolyte microenvironments: a structure-making microenvironment formed by Cd<sup>2+</sup> bound tightly within a hydrogen-bonded H<sub>2</sub>O network (1C electrolyte; Fig. 3i), and a structure-breaking microenvironment created by [CdCl<sub>4</sub>]<sup>2-</sup> within a flexible NH<sub>4</sub><sup>+</sup>-involved hydrogen bonding network (1C6N electrolyte; Fig. 3j).

Subsequently, we performed stepwise DFT simulations for the four solvation shells obtained from previous MD simulations:

[CdCl<sub>4</sub>]<sup>2-</sup>, [Cd(H<sub>2</sub>O)<sub>4</sub>Cl<sub>2</sub>]<sup>0</sup>, [Cd(H<sub>2</sub>O)<sub>5</sub>Cl]<sup>+</sup>, and [Cd(H<sub>2</sub>O)<sub>6</sub>]<sup>2+</sup>, as seen in Fig. 3k (obtained from Supplementary Figs. 16, 17, 35, 36 and Tables 25–32). The results revealed that the primary [CdCl<sub>4</sub>]<sup>2-</sup> species in the 1C6N electrolyte exhibited the lowest binding energy of −135.327 kcal mol<sup>−1</sup>, while the primary [Cd(H<sub>2</sub>O)<sub>6</sub>]<sup>2+</sup> species in the 1C electrolyte showed the highest binding energy of −300.120 kcal mol<sup>−1</sup> (Fig. 3k). They indicated that the low binding energy of tetrahedral [CdCl<sub>4</sub>]<sup>2-</sup> facilitates stepwise desolvation/solvation processes, contributing to the significantly faster reaction kinetics for the [CdCl<sub>4</sub>]<sup>2-</sup>/Cd couple compared to the [Cd(H<sub>2</sub>O)<sub>6</sub>]<sup>2+</sup>/Cd couple. Furthermore, from the perspective of mass transfer, the high charge density of structure-breaking Cd<sup>2+</sup> resulted in strong the ion-dipole interaction, extending even to the outer-shell H<sub>2</sub>O molecules (DFT modeling: assuming one inner-shell H<sub>2</sub>O corresponds to 2 outer-shell H<sub>2</sub>O molecules). This was evidenced by the high binding energy of 215.771 kcal mol<sup>−1</sup> between the inner-shell H<sub>2</sub>O and the outer-shell H<sub>2</sub>O for the [(Cd(H<sub>2</sub>O)<sub>6</sub>(H<sub>2</sub>O)<sub>12</sub>)]<sup>2+</sup> (Fig. 3l), which restricted the rapid mass transfer process. In contrast, [CdCl<sub>4</sub>]<sup>2-</sup>, similar to [AuCl<sub>4</sub>]<sup>−</sup> as a structure breaker<sup>43</sup>, features a largely tetrahedral geometry and lower charge density, which reduces interactions with surrounding H<sub>2</sub>O molecules and facilitates rapid mass transfer. It was further reflected in the low binding energy (less bound) between inner [CdCl<sub>4</sub>]<sup>2-</sup> shell and outer H<sub>2</sub>O molecules, which exhibited a low binding energy of −132.211 kcal mol<sup>−1</sup> (DFT modeling: assuming one inner-shell Cl<sup>−</sup> corresponds to two outer-shell H<sub>2</sub>O molecules; Fig. 3m). Additionally, NH<sub>4</sub><sup>+</sup> contributed structure-breaking properties by further disrupting the hydrogen-bond network. Therefore, the dual-structure-breaking effect of NH<sub>4</sub><sup>+</sup> and [CdCl<sub>4</sub>]<sup>2-</sup> in 1C6N electrolyte enhanced the charge transfer kinetics of ACBs.

### Cd plating/stripping behaviors in SBE

Considering that the Cd plating/stripping behavior involved the distinct [CdCl<sub>4</sub>]<sup>2-</sup>/Cd couple (1C6N) compared to the [Cd(H<sub>2</sub>O)<sub>6</sub>]<sup>2+</sup>/Cd couple (1C), we anticipated significant differences in their plating behaviors. To validate this hypothesis and rule out the possible homogeneous effects, Cd plating/stripping behavior was examined on Cu foil substrate (Supplementary Fig. 37), with morphological evolution observed using scanning electron microscopy (SEM; Fig. 4a–c and Supplementary Figs. 38–54). In the 1C system, where the electrochemical plating follows [Cd(H<sub>2</sub>O)<sub>6</sub>]<sup>2+</sup> → Cd<sup>0</sup>, a regular textured morphology was sustained up to a plated areal capacity of 3 mAh cm<sup>−2</sup>; beyond this areal capacity, uncontrolled dendrite growth began (Fig. 4a and Supplementary Fig. 38). In contrast, the plating process involving [CdCl<sub>4</sub>]<sup>2-</sup> → Cd<sup>0</sup> in the 1C6N electrolyte displayed uniform grain growth (Fig. 4b and Supplementary Fig. 39), which contributed to more uniform Cd stripping behavior compared to the mossy morphology seen in the 1C electrolyte (Supplementary Figs. 40–42 and Supplementary Note 7). Furthermore, Cd electrodeposition at higher areal capacities demonstrated a consistent, orderly growth pattern of Cd deposits from 10 to 100 mAh cm<sup>−2</sup> (Fig. 4c), highlighting the high durability of the [CdCl<sub>4</sub>]<sup>2-</sup> → Cd<sup>0</sup> transition in 1C6N electrolyte. However, parallel comparisons of Cd deposits formed in the 1C and 1C6N electrolytes clearly revealed a pronounced dendritic disadvantage in 1C system, whereas 1C6N system demonstrated a notable dendrite-free advantage at high areal capacities (Supplementary Figs. 43–54 and Supplementary Note 7).

Then, we examined the cross-sectional morphologies of Cd deposits using focused ion beam SEM (FIB-SEM) and atomic arrangements with high-angle annular dark-field scanning transmission electron microscopy (HAADF-STEM), as shown in Fig. 4d–h. Study areas on both dendritic and smooth surfaces of Cd deposits were selected and sectioned perpendicular to the substrates for analysis (Supplementary Fig. 55). In the 1C electrolyte, Cd dendrites displayed polycrystalline structures with multiple boundaries, suggesting that dendritic growth involved the formation of new grain boundaries followed by

subsequent grain growth (Fig. 4d). HAADF-STEM images of adjacent regions (1 and 2 in Fig. 4d) confirmed discontinuous atomic arrangements (Fig. 4f, g), denoting differing growth directions of Cd grains and underlying dendrite formation. In contrast, the cross section of Cd deposits in the 1C6N electrolyte exhibited a large, single-crystalline structure without detectable grain boundaries (Fig. 4e). The HAADF-STEM image revealed a uniform hexagonal close-packed (HCP) atomic arrangement (Fig. 4h), where Cd atoms align in an orderly abababab layer-by-layer pattern, achieving dense atomic packing. This growth mode prevents the formation of new grain boundaries and thus suppresses dendrite formation.

Given the intrinsic link between macroscopic electrodeposition behavior and microscopic charge-transfer kinetics, influenced by the electrolyte microenvironment, we directly correlated Cd plating behaviors with charge-transfer kinetics. Previous results demonstrated significantly faster kinetics for [CdCl<sub>4</sub>]<sup>2-</sup> ↔ Cd<sup>0</sup> in the 1C6N electrolyte compared to the relatively slower kinetics of [Cd(H<sub>2</sub>O)<sub>6</sub>]<sup>2+</sup> ↔ Cd<sup>0</sup> in 1C electrolyte, as shown in Figs. 2f–i and 3b, k–m. We believe that this kinetic disparity contributes to the distinct Cd plating behaviors observed: a kinetics-limited system vs. a fast-kinetics system. Specifically, the kinetics-limited 1C system maintained regular grain growth up to an areal capacity of 3 mAh cm<sup>−2</sup>, but dendritic growth emerged at a higher areal capacity of 5 mAh cm<sup>−2</sup> (Fig. 4a). This suggested that the relatively slow charge-transfer kinetics failed to keep pace with the rapid Cd<sup>2+</sup> depletion in the electrode/electrolyte interfacial layer as the plated capacity increased, disrupting the thermodynamic balance required for uniform grain growth (Fig. 4i)<sup>55,56</sup>. As a result, at high plating capacity, Cd growth became kinetics-limited, leading to new grain boundary formation and irregular grain growth (Fig. 4d). Notably, visible dendritic Cd deposit at an areal capacity of 100 mAh cm<sup>−2</sup> was observed in the optical inset of Fig. 4i. In contrast, in the 1C6N electrolyte, the fast mass transfer, and effortless desolvation and plating behavior ([CdCl<sub>4</sub>]<sup>2-</sup> → Cd<sup>2+</sup> → Cd<sup>0</sup>) facilitated Cd grain growth without kinetics limitations, thus maintaining the growth of Cd grain at thermodynamic equilibrium<sup>56,57</sup>. This process resulted in the controlled and regular grain formation (Fig. 4j). Even at an areal capacity of 100 mAh cm<sup>−2</sup>, the Cd deposit still exhibited a densely packed grain arrangement, as shown in the optical inset of Fig. 4j. However, once structure maker was introduced, even though 1C6L system contained the fast-kinetics structure breaker of [CdCl<sub>4</sub>]<sup>2-</sup>, the presence of 6 m structure-making Li<sup>+</sup> significantly hindered charge-transfer kinetics, leading to severe dendrite formation at an areal capacity of 10 mAh cm<sup>−2</sup> (Supplementary Figs. 56, 57, Supplementary Note 8). Thus, the SBE addressed dendritic issue under deep cycling. By the way, we observed that replicating the success of the SBE in AZBs proved challenging (see details in Supplementary Figs. 58–63 and Supplementary Note 9), which further highlights the uniqueness of our proposed system.

### Electrochemical performance of Cd electrodes

We further confirmed that the SBE electrolyte enabled durable Cd plating/stripping stability at a high areal capacity (5 mAh cm<sup>−2</sup>) and high NEU (55%) for practical applications<sup>58</sup>. Performance comparisons were shown in Fig. 5a, b, and Supplementary Fig. 64. The SBE achieved an initial CE of 99.50% and an average CE of 99.93% over 300 cycles, with highly consistent plating/stripping profiles, indicating high Cd plating/stripping efficiency. In contrast, the 1C system exhibited an initial CE of 98.89% and an average CE of 99.86% over 39 reversible cycles, after which sudden cell shorting and failure occurred at the 40th cycle (Supplementary Fig. 64a, b). To figure out the high reversibility of the Cd electrode in 1C6N electrolyte, we analyzed post-cycling electrode morphologies using X-ray diffraction (XRD) and SEM. The Cd electrode (1C6N) displayed (101) plane-dominant and tightly stacked texture (Fig. 5c, d; as illustrated in the schematic of Fig. 5e). In



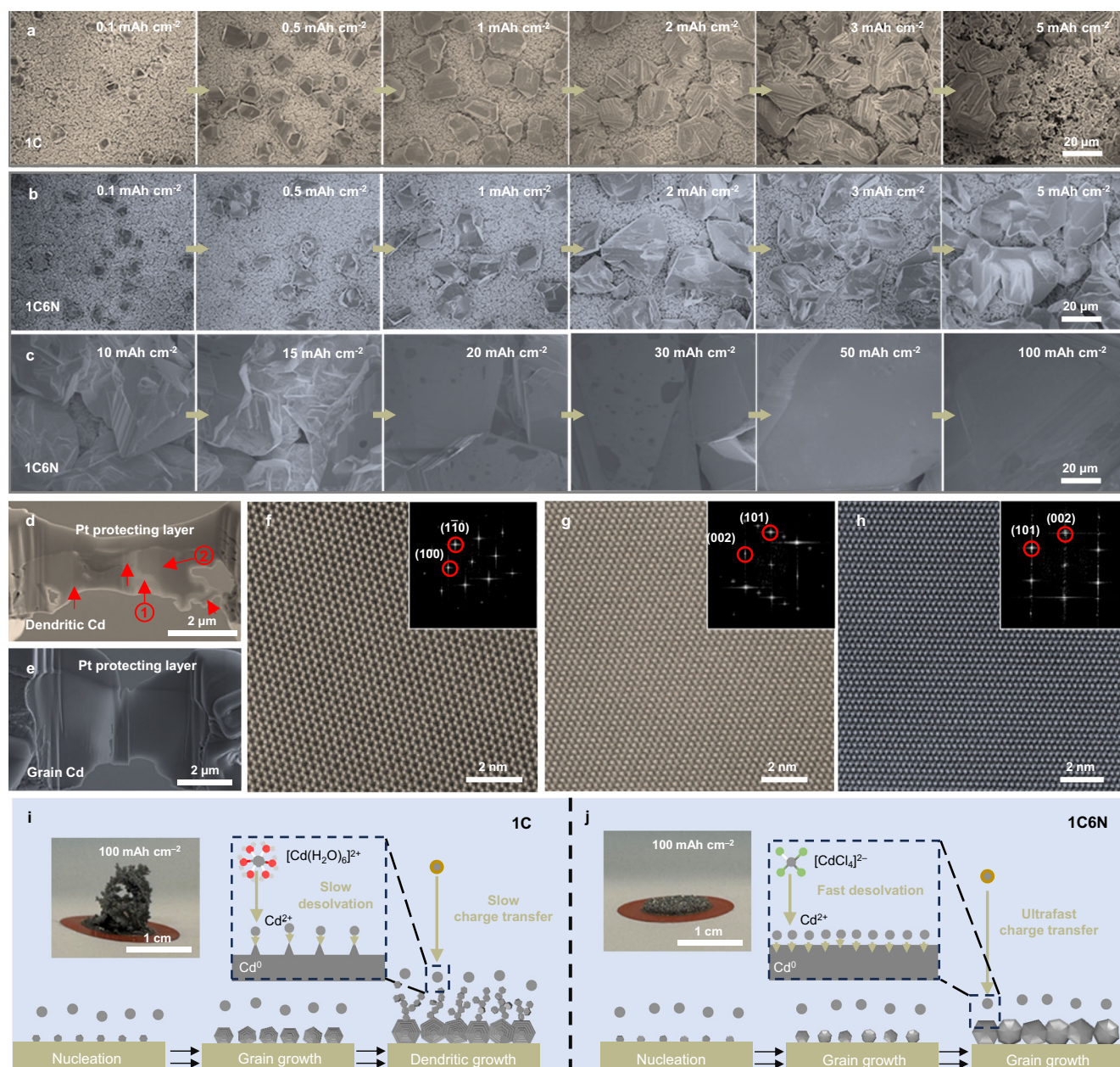


**Fig. 4 | Kinetics-controlled Cd plating behavior.** SEM images of Cd deposits at a current density of 10 mA cm<sup>-2</sup> with increasing areal capacities: from 0.1 to 5 mAh cm<sup>-2</sup> in 1C electrolyte (a), from 0.1 to 5 mAh cm<sup>-2</sup> in 1C6N electrolyte (b), and from 10 to 100 mAh cm<sup>-2</sup> in 1C6N electrolyte (c). Cd electrodeposition was carried out at an average temperature of 25 ± 2 °C. FIB-SEM images of cross-section Cd deposits in 1C electrolyte (d) and 1C6N electrolyte (e) with an areal capacity of 5 mAh cm<sup>-2</sup>. f, g HAADF-STEM images of cross-sectional Cd deposits in 1C

electrolyte at a current density of 10 mA cm<sup>-2</sup> with an areal capacity of 5 mAh cm<sup>-2</sup>, corresponding FFT patterns shown in insets. h HAADF-STEM image of cross-sectional Cd deposit in 1C6N electrolyte at a current density of 10 mA cm<sup>-2</sup> with an areal capacity of 5 mAh cm<sup>-2</sup>, corresponding FFT pattern shown in inset. Schematic of kinetics-controlled Cd plating behaviors in 1C electrolyte (i) and 1C6N electrolyte (j). Insets: optical morphologies of Cd deposits at a current density of 10 mA cm<sup>-2</sup> and an areal capacity of 100 mAh cm<sup>-2</sup> in 1C electrolyte (i) and 1C6N electrolyte (j).

contrast, the Cd electrode (1C) showed random crystal orientations and irregular plate-like textures (Fig. 5c and Supplementary Fig. 65), which could easily lead to cell shorting. In addition, comparative Cd||Cu cells using 1C6L, 1M CdSO<sub>4</sub>, 1M CdSO<sub>4</sub> + 2M Li<sub>2</sub>SO<sub>4</sub>, and 1M CdSO<sub>4</sub> + 3M (NH<sub>4</sub>)<sub>2</sub>SO<sub>4</sub> electrolytes further highlighted the superiority of the dual structure-breaking system, as evidenced by the poor Cd plating/stripping capability of the other electrolyte systems (Supplementary Figs. 66, 67 and Supplementary Note 10). Consequently, the dendrite-free capability of the SBE provided highly electrochemical reversibility for the Cd electrode, further evidenced by a reversible Cd||Cu cell at a higher areal capacity of 15 mAh cm<sup>-2</sup>, which exhibited a

consistently regular Cd texture (Supplementary Figs. 68, 69 and Supplementary Note 11).

Given that energy storage applications inherently require intermittent operation and long-term storage, high corrosion resistance is essential for ACBs. This necessity was first assessed via acidic corrosion testing (Supplementary Fig. 70). However, based on the Pourbaix diagram of Cd and H<sub>2</sub>O (Supplementary Fig. 71 and Supplementary Note 12), we noted that the redox potential of the [CdCl<sub>4</sub>]<sup>2-</sup>/Cd couple in the 1C6N electrolyte was lower than that of the HER, and the addition of NH<sub>4</sub>Cl reduced the pH of electrolytes from 5.32 in 1C to 3.68 in 1C6N, posing a potential corrosion risk for the Cd electrode.

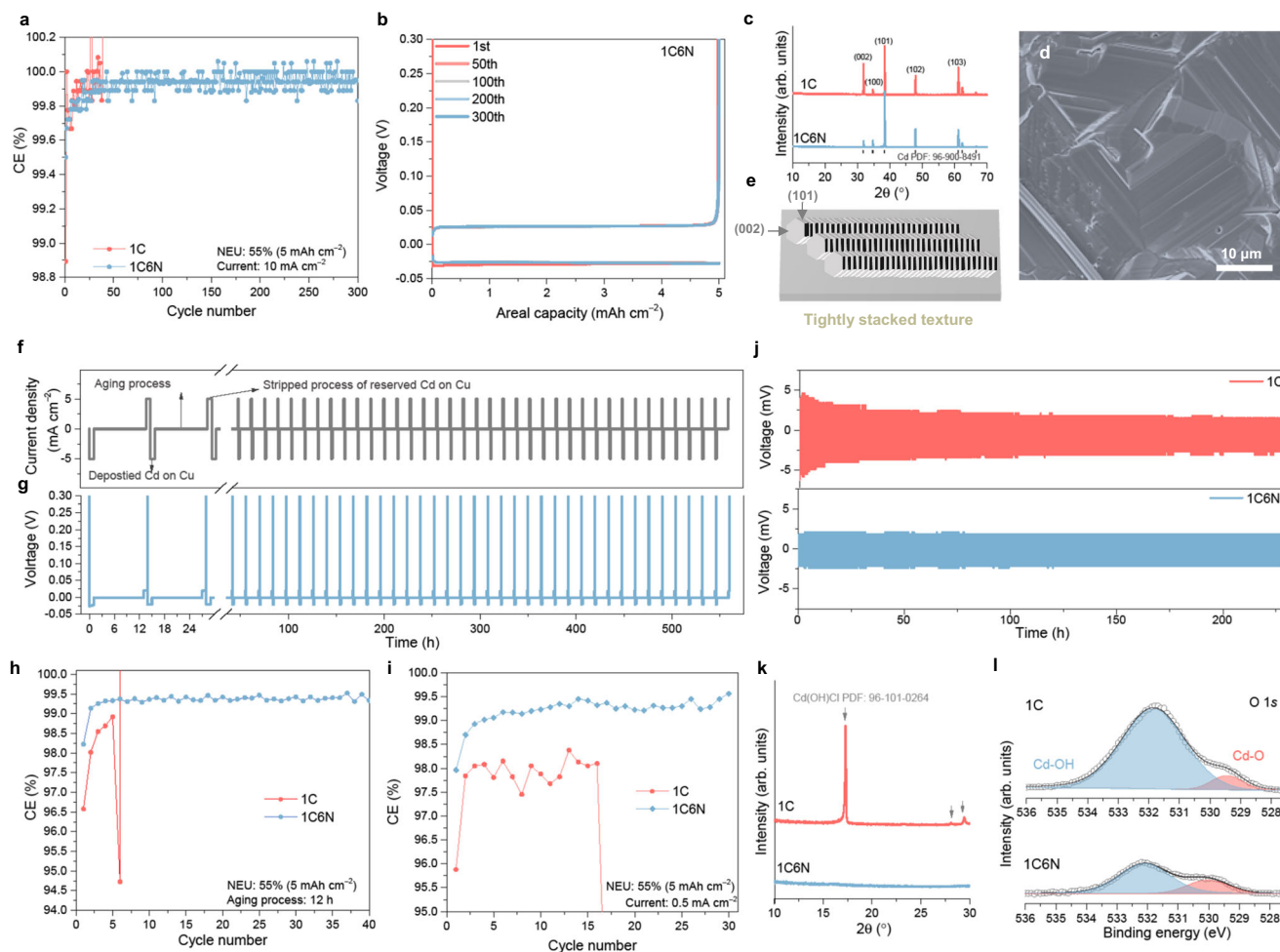


**Fig. 5 | Corrosion-resistant and dendrite-free Cd electrode.** CEs of Cd||Cu cells in different electrolytes measured at  $10 \text{ mA cm}^{-2}$  and  $5 \text{ mAh cm}^{-2}$  with a NEU of 55% (a) and the corresponding Cd plating/stripping curves in 1C6N electrolyte (b). XRD patterns of Cd electrodes in 1C and 1C6N electrolytes after cycling 10 cycles (c), SEM image in 1C6N electrolyte (d) and the schematic of stacked Cd texture (e). Aging CE test sequence (f), the corresponding voltage profiles in 1C6N electrolyte (g), and aging CEs in different electrolytes (h). Aging CE performed at a fixed plated capacity of  $5 \text{ mAh cm}^{-2}$  and current density of  $5 \text{ mA cm}^{-2}$ , an aging time of 12 h, and

then a stripped current density of  $5 \text{ mA cm}^{-2}$  for per cycle with a NEU of 55% (f–h). i CEs of Cd||Cu cells in different electrolytes measured at  $0.5 \text{ mA cm}^{-2}$  and  $5 \text{ mAh cm}^{-2}$  with a NEU of 55%. j Voltage curves of Cd||Cd symmetric cells in different electrolytes at  $0.5 \text{ mA cm}^{-2}$  and  $0.1 \text{ mAh cm}^{-2}$ . An average electrochemical testing temperature of  $25 \pm 2^\circ \text{C}$  was maintained in (a, b, f–j). XRD patterns (k) and XPS spectra of O 1s (l) of Cd electrodes after Cd plating/stripping for 229 h in Cd||Cd cells.

Interestingly, despite these factors, the Cd electrode in the SBE exhibited high corrosion resistance. We evaluated the aging CE of the Cd electrode under intermittent use, as shown in Fig. 5f. The results indicated that intermittent storage of metallic Cd in the SBE did not lead to capacity loss from corrosion, as confirmed by stable voltage polarization curves for plating, aging, and stripping processes (Fig. 5g), a high average CE of 99.34% (Fig. 5h), and highly consistent plating/stripping curves over multiple cycles (Supplementary Fig. 72a). In contrast, while the Cd electrode in the 1C electrolyte was cycled only 6 cycles, its failure was attributed to cell shorting rather than corrosion (Supplementary Fig. 72b, c). Notably, it still achieved a relatively high average aging CE of 97.58% (Fig. 5h), though slightly lower than that of the 1C6N system, indicating a somewhat lower corrosion resistance compared to the SBE system.

The aging CE primarily evaluated the long-term storage capability of the Cd negative electrode in aqueous medium. To further assess electrochemistry-induced corrosion, HER, we investigated the Cd plating/stripping CE at a low current density of  $0.5 \text{ mA cm}^{-2}$ , as suggested by Ji and Nazar<sup>59</sup>, with a high areal capacity of  $5 \text{ mAh cm}^{-2}$  and high NEU of 55% in Cd||Cu cells; in other words, the highly reversible Cd plating/stripping behavior under low current density, high areal

capacity and high NEU offers a more compelling demonstration of its corrosion-resistant capability. The results indicated that the Cd plating/stripping behavior in the 1C6N electrolyte achieved a high average CE of 99.24% (Fig. 5i) with highly consistent voltage polarization curves (Supplementary Fig. 73a, b), in contrast to the limited reversibility observed in the 1C electrolyte (Fig. 5i and Supplementary Fig. 73c, d). It indicated that the SBE imparted electrochemical corrosion resistance to Cd electrodes. Furthermore, the post-cycling electrode morphologies at low current density mirrored those in Fig. 5a: the 1C6N system exhibited a (101) plane-dominant and regular texture, while the 1C system showed an irregular plate-like texture (Supplementary Figs. 74 and 75), illustrating the difference in cycling lifespan determined by these distinct plating/stripping behaviors. In addition, post-cycling XRD analysis revealed the formation of Cd(OH)Cl by-products on the Cd electrode in the 1C electrolyte, likely due to HER facilitated under low current conditions ( $\text{Cd}^{2+} + \text{H}_2\text{O} + \text{Cl}^- + \text{e}^- \rightarrow \text{Cd(OH)Cl} + \text{H}_2$ ), whereas no such by-product was detected in the 1C6N system (Supplementary Fig. 75). This finding with high CE further underscored that, due to fast kinetics in the SBE, HER was effectively suppressed.

The Cd||Cd symmetric cells reinforced this corrosion-resistant conclusion by applying continuous low-current fluctuations to induce



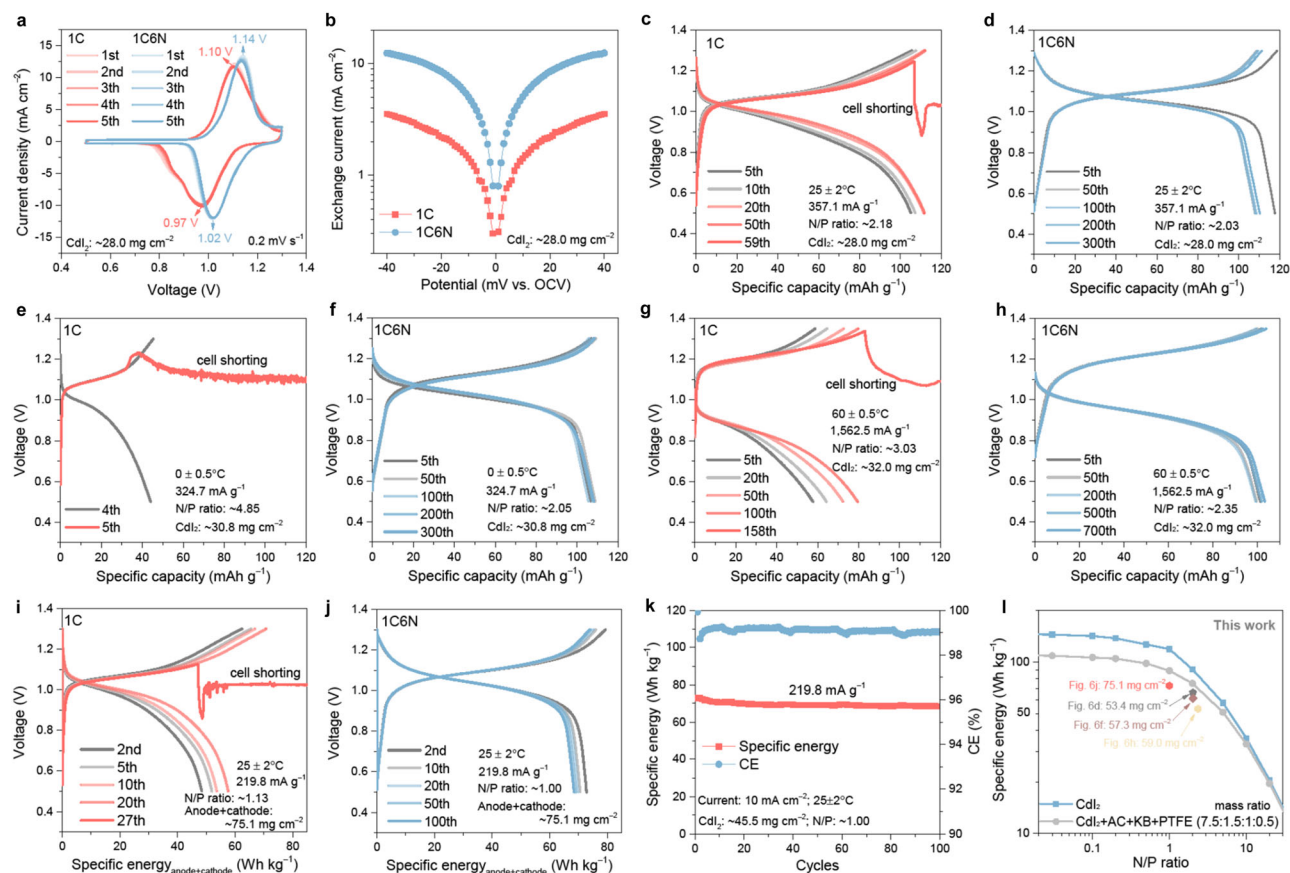


**Fig. 6 | Rechargeable capability of high-loading Cd||CdI<sub>2</sub> full cells in 1C and 1C6N electrolytes.** **a** CV curves of 5 cycles at a scan rate of 0.2 mV s<sup>-1</sup> in 1C and 1C6N electrolytes at 25 ± 2 °C. **b** Exchange currents in 1C and 1C6N electrolytes at 25 ± 2 °C. Charge/discharge cruces in 1C electrolyte (**c**) and 1C6N electrolyte (**d**) at 25 ± 2 °C and 357.1 mA g<sup>-1</sup> (10 mA cm<sup>-2</sup>). Charge/discharge cruces in 1C electrolyte (**e**) and 1C6N electrolyte (**f**) at 0 ± 0.5 °C and 324.7 mA g<sup>-1</sup> (10 mA cm<sup>-2</sup>). Charge/discharge cruces in 1C electrolyte (**g**) and 1C6N electrolyte (**h**) at 60 ± 0.5 °C and 1,562.5 mA g<sup>-1</sup> (50 mA cm<sup>-2</sup>). Charge/discharge cruces in 1C electrolyte (**i**) and 1C6N

electrolyte (**j**) at 25 ± 2 °C and 219.8 mA g<sup>-1</sup> (10 mA cm<sup>-2</sup>) with a high CdI<sub>2</sub> loading ~45.5 mg cm<sup>-2</sup> and total negative and positive electrode mass of ~75.1 mg cm<sup>-2</sup>. **k** Corresponding cycling performance in 1C6N electrolyte at a low N/P ratio of ~1.00. **l** Comparison between practical and theoretical specific energies of Cd||CdI<sub>2</sub> full cells, calculated based on the total mass loading (including Cd foil, CdI<sub>2</sub>, AC, KB, and binder) of both negative and positive electrodes: 53.4 mg cm<sup>-2</sup> (**d**), 57.3 mg cm<sup>-2</sup> (**f**), 59.0 mg cm<sup>-2</sup> (**h**), 75.1 mg cm<sup>-2</sup> (**j**).

HER (Fig. 5j)<sup>39,60</sup>. Stable and minimal voltage fluctuations were observed over 229 h in both 1C and 1C6N electrolytes. However, in the 1C electrolyte, fine crystalline Cd(OH)Cl particulates formed on the Cd electrode surface, contrasting with the smooth Cd electrode in the 1C6N electrolyte (Fig. 5k and Supplementary Fig. 76). Further analysis with X-ray photoelectron spectroscopy (XPS) revealed that these corrosive compounds covered the entire Cd electrode surface in the 1C electrolyte, while the shallow surface layers on the Cd electrode (1C6N) were attributed to slight air oxidation or mild electrochemical corrosion (Fig. 5l and Supplementary Fig. 77). Therefore, this range of experiments and detailed characterizations confirmed that the fast-kinetics SBE effectively suppressed corrosion reactions. To advance scientific understanding, we further explored the limits of Cd corrosion resistance in the SBE (Supplementary Fig. 78 and Supplementary Note 12) and verified the incompatibility of this SBE with AZB systems through parallel comparisons (see discussions in Supplementary Figs. 79–87 and Supplementary Note 13).

### Electrochemical performance of full cells

The electrochemical performance of ACBs was evaluated using commercially available positive electrode materials without process optimization. These materials included coordination-type PANI, capacitance-type AC, intercalation-type V<sub>2</sub>O<sub>5</sub>, and conversion-type CdI<sub>2</sub>, paired with the durable Cd negative electrode and SBE, and

benchmarked against full cells with the 1C electrolyte. CV profiles of the high-loading Cd||CdI<sub>2</sub> full cells were initially collected to examine electrochemical behaviors (Fig. 6a). Due to the lower redox potential of the [CdCl<sub>4</sub>]<sup>2-</sup>/Cd couple compared to the [Cd(H<sub>2</sub>O)<sub>6</sub>]<sup>2+</sup>/Cd couple, while matching the I<sub>2</sub>/I<sup>-</sup> couple at 0.54 V vs. SHE as the positive electrode, the full cell in the 1C6NH<sub>4</sub> electrolyte exhibited higher reduction (1.02 V) and oxidation (1.14 V) voltages than the cell in the 1C electrolyte. Additionally, the cell with the 1C6N electrolyte showed a higher response current, indicating the faster reaction kinetics. This was further validated by the increased exchange current of the full cell with the 1C6N electrolyte (Fig. 6b and Supplementary Fig. 88).

This kinetics disparity was particularly reflected in the charge/discharge profiles of the full cells operated at a specific current of 357.1 mA g<sup>-1</sup> (current density: 10 mA cm<sup>-2</sup>) at an average testing temperature of 25 ± 2 °C, as shown in Fig. 6c, d. In the 1C electrolyte, the restricted mass transport and the sluggish reaction kinetics within the high-loading positive electrode caused the discharge plateau of the full cell to vanish, leading to smoothly curved discharge profiles and premature cell failure due to cell shorting (Fig. 6c and Supplementary Fig. 89a). In contrast, the SBE facilitated accelerated reaction processes at both the negative and positive electrodes, driven by the rapid charge-transfer kinetics. It enabled the full cell with the 1C6N electrolyte to sustain a stable discharge plateau above 1.00 V, even with a high-loading CdI<sub>2</sub> positive electrode of ~28.0 mg cm<sup>-2</sup> and low

negative-to-positive capacity (N/P) ratio of  $\sim 2.03$  (Fig. 6d). Additionally, it exhibited durable rechargeability retaining  $\sim 92\%$  of its initial capacity after 300 cycles (Supplementary Fig. 89b).

Furthermore, this performance gap widened significantly at a low average testing temperature of  $0 \pm 0.5^\circ\text{C}$ . The full cell with the 1C electrolyte delivered a limited discharge capacity of just  $44\text{ mAh g}^{-1}$ , with cell shorting occurring after only five charge cycles due to severely impeded reaction kinetics at low temperatures (Fig. 6e and Supplementary Fig. 90a). In contrast, despite slight reductions in both the discharge plateau and specific capacity, the SBE showed minimal impact on charge-transfer kinetics under low-temperature conditions (Fig. 6f and Supplementary Fig. 90b). It achieved durable cycling over 300 cycles with a high-loading  $\text{CdI}_2$  positive electrode of  $30.8\text{ mg cm}^{-2}$  and low N/P ratio of  $\sim 2.05$ , maintaining a high-capacity retention of  $\sim 94\%$  over 300 cycles. Considering the exchange current in the 1C6N electrolyte approached its limit at an average testing temperature of  $60^\circ\text{C} \pm 0.5^\circ\text{C}$ , while the 1C electrolyte exhibited unstable exchange current beyond  $60 \pm 0.5^\circ\text{C}$  (Fig. 3b), we further evaluated the rechargeable performance of full cells at an average temperature of  $60 \pm 0.5^\circ\text{C}$  under a high specific current of  $1,562.5\text{ mA g}^{-1}$  (current density:  $50\text{ mA cm}^{-2}$ ), as shown in Fig. 6g, h. Notably, the elevated temperature did not enhance the fast charge/discharge stability of the full cell in the 1C electrolyte at an increased specific current. In contrast, the high-loading full cell with a low N/P ratio in the 1C6N electrolyte sustained durable operation over 700 cycles at a high specific current, maintaining negligible capacity fading and showing a discharge capacity of  $\sim 100\text{ mAh g}^{-1}$  (Fig. 6h and Supplementary Fig. 91).

To satisfy the specific energy requirements of energy storage systems, such as  $40\text{ Wh kg}^{-1}$ <sup>58</sup>, we further evaluated the rechargeable capability of full cells with a lower N/P ratio of  $\sim 1.00$  and a higher  $\text{CdI}_2$  loading of  $45.5\text{ mg cm}^{-2}$  (Fig. 6i–k). Unlike the poor rechargeability seen with the 1C electrolyte (Fig. 6i and Supplementary Fig. 92), the full cell with the 1C6N electrolyte achieved a high specific energy of  $72.9\text{ Wh kg}^{-1}$ , calculated based on the total negative and positive electrode mass, including the inactive binder and conductive carbon (Fig. 6j), and demonstrated stable cycling over 100 cycles with a capacity retention of  $\sim 94\%$  (Fig. 6k). In addition, all  $\text{Cd}||\text{CdI}_2$  full cells, presented here, exhibited acceptable specific energies based on the total mass of negative and positive electrodes, specifically  $66.3\text{ Wh kg}^{-1}$  ( $25 \pm 2^\circ\text{C}$ ,  $357.1\text{ mA g}^{-1}$ ; Fig. 6d),  $61.5\text{ Wh kg}^{-1}$  ( $0 \pm 0.5^\circ\text{C}$ ,  $324.7\text{ mA g}^{-1}$ ; Fig. 6f), and  $53.4\text{ Wh kg}^{-1}$  ( $60 \pm 0.5^\circ\text{C}$ ,  $1,562.5\text{ mA g}^{-1}$ ; Fig. 6h), as summarized in Fig. 6l. These results indicated the potential of  $\text{Cd}||\text{CdI}_2$  full cells for practical energy storage applications.

On the other hand, ACBs assembled with the SBE demonstrated compatibility across various types of positive electrodes. For instance, coordination-type  $\text{Cd}||\text{PANI}$  full cells with the 1C6N electrolyte exhibited improved rechargeability under diverse conditions, including the low specific current ( $145.3\text{ mA g}^{-1}$ ), high specific current ( $6,544.5\text{ mA g}^{-1}$ ), low N/P ratio (1.91), high positive electrode loading ( $38.22\text{ mg cm}^{-2}$ ), and intermittent usage (see details in Supplementary Figs. 93–98). The capacitance-type  $\text{Cd}||\text{AC}$  hybrid capacitor displayed typical characteristics of electric double-layer capacitors, with large response currents at scan rates ranging from 20 to  $100\text{ mV s}^{-1}$ , and achieved high rechargeability, retaining  $\sim 90\%$  capacity after 10,000 cycles (Supplementary Fig. 99). Lastly, the ACB with an intercalation-type  $\text{V}_2\text{O}_5$  positive electrode demonstrated rechargeable capability, delivering a high discharge capacity of  $270\text{ mAh g}^{-1}$  after 100 cycles (Supplementary Fig. 100).

### Practicality of ACBs

To evaluate the practical ACBs with the SBE, we further assembled a scaled-up  $\text{Cd}||\text{CdI}_2$  full cell using a  $\text{CdI}_2$  positive electrode, a glass fiber membrane soaked in 1C6N electrolyte, and a Cd foil negative electrode within an enlarged cell mold (Fig. 7a), which powered an LED light (Fig. 7b). This scaled-up cell featured a large active area of  $49\text{ cm}^2$

( $7\text{ cm} \times 7\text{ cm}$ ) for both the negative and positive electrodes, with a high-loading  $\text{CdI}_2$  of  $1.1\text{ g}$  ( $22.45\text{ mg cm}^{-2}$ ) on the positive electrode. Despite its size, the cell still performed a stable discharge voltage of  $\sim 1.00\text{ V}$ , a discharge capacity of  $\sim 120\text{ mAh g}^{-1}$ , minimal polarization ( $\sim 0.15\text{ V}$ ), and consistent charge/discharge profiles over multiple cycles (Fig. 7c, e). This performance highlighted the ability of SBE to enable rapid charge-transfer kinetics, allowing two full cells connected in series to deliver a combined discharge voltage of  $\sim 2.00\text{ V}$ , with a discharge specific capacity comparable to that of a single cell (Fig. 7c). In contrast, the full cell with the 1C electrolyte exhibited significant voltage polarization and limited cycling (Fig. 7c, d). Additionally, the scaled-up cell with 1C6N electrolyte demonstrated high rechargeability, maintaining a discharge capacity of  $\sim 120\text{ mAh g}^{-1}$  with high-capacity retention of  $\sim 97\%$  over 300 charge/discharge cycles spanning  $\sim 1586\text{ h}$  (Fig. 7f). It indicated the robustness and practicality of ACBs. Further optimization of cell components could unlock new opportunities, establishing ACBs as a promising candidate for next-generation energy storage applications.

It is important to note that due to their geochemical affinity, Cd and Zn rarely occur as discrete minerals but are primarily co-located in major sphalerite deposits. Consequently, Cd recovery is an inevitable by-product of Zn refining—wherever Zn is extracted, Cd is also present<sup>33,34</sup>. As metallic Zn refinement inherently involves concurrent Cd processing, the accelerating demand for Zn mining and refining driven by the development of AZBs as future energy storage systems will similarly increase Cd production (Fig. 7g). This presents an opportunity for utilizing extracted Cd resources to advance ACB development based on the expectable specific energy of practical energy storage applications (Supplementary Fig. 101 and Supplementary Note 14). More importantly, although ACBs sacrifice some specific energy compared to AZBs, they exhibit superior corrosion resistance and stability—advantages not inherent to Zn negative electrode—delivering efficient electrochemical performance through simple electrolyte optimization. However, it is crucial to emphasize that Cd metal and its compounds are toxic, rendering them unsuitable for everyday consumer electronics unless comprehensive protective measures are implemented. Instead, as illustrated in Fig. 7g, ACBs could be envisioned for applications such as grid storage, wind and solar energy storage, and industrial energy storage, as well as the charging station. Furthermore, advancements in battery manufacturing and recycling technologies could help mitigate or even resolve toxicity concerns.

## Discussion

In summary, we developed a fast-kinetics and durable ACB enabled by a low-cost and quasi-neutral SBE. The dual structure breakers,  $\text{NH}_4^+$  and  $[\text{CdCl}_4]^{2-}$ , imparted rapid kinetics to the ACB system, effectively addressing two issues commonly found in metallic negative electrode-based batteries: dendritic growth and corrosion. As a result, the Cd electrode achieved a compelling CE of  $99.93\%$  and an aging CE of  $99.34\%$  for plating/stripping at a high NEU of  $55\%$  (areal capacity:  $5\text{ mAh cm}^{-2}$ ). Furthermore, the fast-kinetics ACB demonstrated high compatibility with various positive electrode materials, including  $\text{CdI}_2$ , PANI, AC, and  $\text{V}_2\text{O}_5$ . These findings demonstrated the potential of SBE-based ACBs to advance aqueous metal battery concepts. Promising full-cell performance at high loadings and low N/P ratios underscores their practicality and commercial promise.

## Methods

### Materials

Cadmium chloride ( $\text{CdCl}_2$ , 99.99%), ammonium chloride ( $\text{NH}_4\text{Cl}$ , 99.99%), zinc sulfate heptahydrate ( $\text{ZnSO}_4 \cdot 7\text{H}_2\text{O}$ , 99%), sodium chloride ( $\text{NaCl}$ , 99%), lithium chloride ( $\text{LiCl}$ , 99%), potassium chloride ( $\text{KCl}$ , 99%), magnesium chloride ( $\text{MgCl}_2$ , 98%), zinc chloride ( $\text{ZnCl}_2$ , 98%), isopropanol (anhydrous, 99.5%), cadmium iodide ( $\text{CdI}_2$ , 99%), vanadium (V) oxide ( $\text{V}_2\text{O}_5$ , 99.95%), polyaniline (PANI, average  $M_w$ :

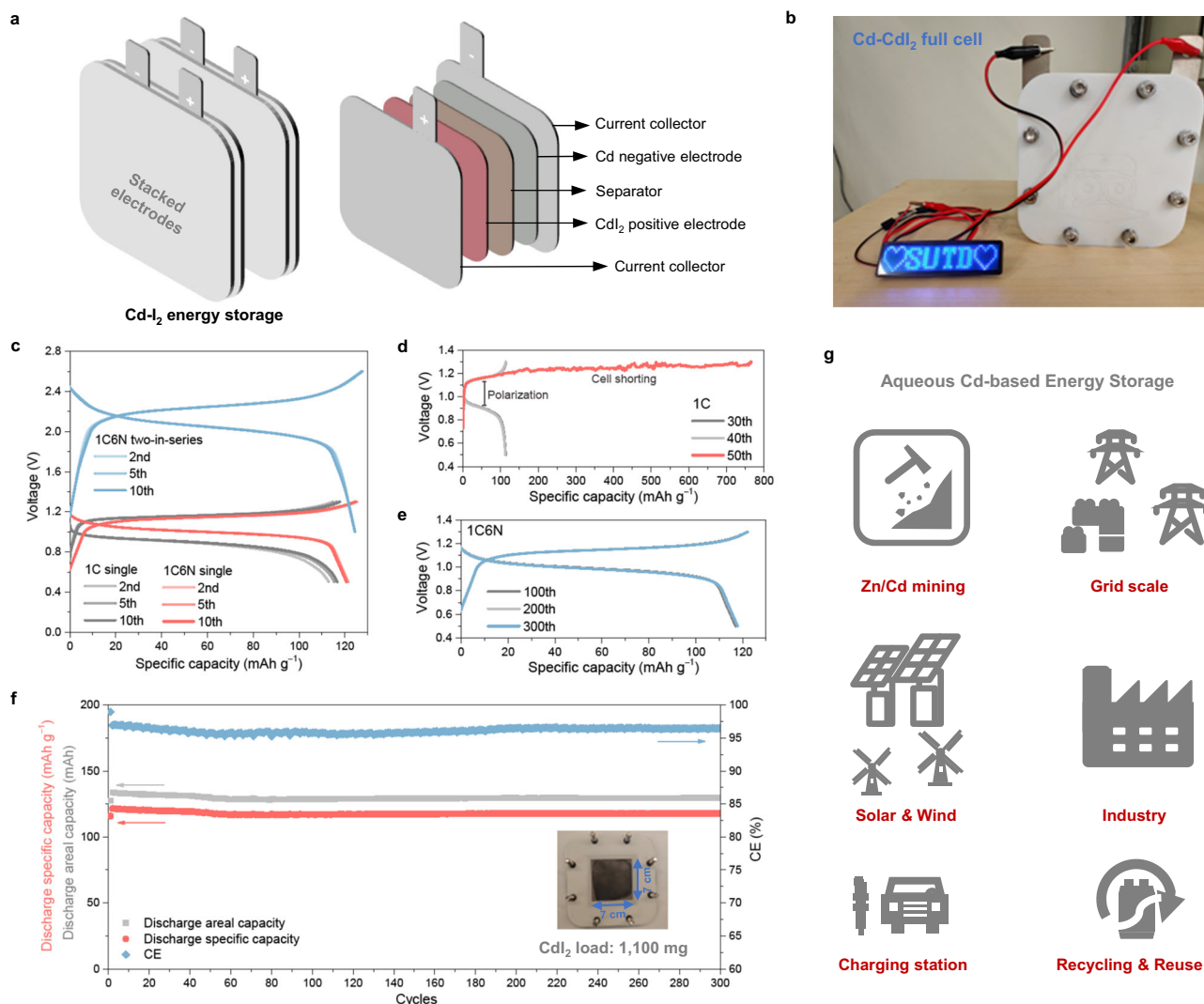


**Fig. 7 | Practicality of ACBs.** **a** Schematic diagram of the scaled-up Cd||CdI<sub>2</sub> full cell. **b** Illustration of scaled-up Cd||CdI<sub>2</sub> full cell powering the LED light. **c** Charge/discharge curves of single and two-in-series scaled-up Cd||CdI<sub>2</sub> full cell in 1C and 1C6N electrolytes at 50 mA. Charge/discharge curves of single scaled-up Cd||CdI<sub>2</sub> full

cells in 1C electrolyte (**d**) and 1C6N electrolyte (**e**) at 50 mA. **f** The corresponding cycling performance in 1C6N electrolyte. Inset: photograph of the scaled-up CdI<sub>2</sub> positive electrode. An average testing temperature of  $25 \pm 2^\circ\text{C}$  was maintained in (**c–f**). **g** Mining, applications, and recycling of the ACBs.

-100,000) and sulfuric acid (H<sub>2</sub>SO<sub>4</sub>, 95%–97%) were obtained from Sigma Aldrich. Cd foil (99.9%), Zn foil (99.9%), and polytetrafluoroethylene (PTFE) aqueous dispersion solution (D-210C, solid content: 60 w%, size:  $\sim 0.25\ \mu\text{m}$  size) were obtained from the supplier of SCI Materials Hub. Activated carbon (AC, YP80F), conductive carbon (Ketjen black; KB), copper (Cu) foil (MA-EN-CU-0002, thickness: 9  $\mu\text{m}$ , purity: >99%), titanium (Ti) mesh (MA-EN-CU-0017, purity: >99%, pore size: 100 mesh, thickness: 0.27 mm thickness, areal density:  $\sim 26.5\ \text{mg cm}^{-2}$ ) and graphite (MA-EN-AN-0019) were obtained from the Canrd New Energy Technology.

### Preparation of electrodes

**Cd and Zn electrodes preparation:** metallic electrodes were achieved by continuously rolling of commercial Zn and Cd foils through a roll press (MSK-2150-H5) until the required areal capacity of Cd and Zn electrodes in detailed cells were attained, which were subsequently cut into circular foils with a diameter of 1 cm for electrode usage of Swagelok cell, as shown in Supplementary Table 33. V<sub>2</sub>O<sub>5</sub> positive electrode preparation: Commercial V<sub>2</sub>O<sub>5</sub> and graphite powders were mixed at a mass ratio of 8:2 and loaded into an 80 mL agate grinding bowl along with agate balls (diameter: 40 mm), using a ball-to-powder

mass ratio of 3:1. The total mass of the solid mixture was 10 g. The mixture was subjected to ball milling using a FRITSCH planetary mono Mill (Pulverisette 6) at a rotation speed of 500 rpm for a total duration of 480 min, with an interval mode of 25 min milling followed by 5 min rest. Subsequently, the V<sub>2</sub>O<sub>5</sub> positive electrode was prepared by manually grinding the ball-milled V<sub>2</sub>O<sub>5</sub>/graphite mixture, KB, and PTFE in a mass ratio of 8:1:1 in isopropanol using an agate mortar and pestle until a uniform and clay-like consistency was achieved. Finally, the resulting pliable mixture was pressed into Ti mesh through a roll press (MSK-2150-H5) and dried in the vacuum oven at  $80^\circ\text{C}$  for 8 h. Preparation of PANI, AC and CdI<sub>2</sub> positive electrodes: the PANI positive electrode was prepared by manually grinding the commercial PANI, KB and PTFE in a mass ratio of 7:2:1 in isopropanol using an agate mortar and pestle, until a uniform and clay-like consistency was achieved. Finally, the material mixture was pressed into Ti mesh through a roll press (MSK-2150-H5) and dried in the vacuum oven at  $80^\circ\text{C}$  for 8 h. Preparation of AC positive electrode is similar to PANI positive electrode, where the difference lies in the mass ratio of AC: KB: PTFE is 8:1:1. Preparation of CdI<sub>2</sub> positive electrode is also similar to PANI positive electrode, where the difference lies in the mass ratio of CdI<sub>2</sub>: AC: KB: PTFE is 7.5:1.5:1:0.5. Finally, all the positive electrodes for the usage of



Swagelok cells were cut into circular electrodes with a diameter of 1 cm. For the scaled-up full cell, the Cd foil negative electrode (100  $\mu\text{m}$  thickness, obtained by rolling) and  $\text{CdI}_2$  positive electrode ( $\text{CdI}_2$  loading:  $22.45 \text{ mg cm}^{-2}$ ) were cut into a  $7 \times 7 \text{ cm}$  square for subsequent cell assembly. Corresponding loadings of the positive electrodes are clearly indicated in the corresponding figures or captions of Manuscript and Supplementary Information. All the current collectors used in this work were employed without any additional treatments. Except for the necessary drying steps to remove residual solvents, all electrodes were prepared under a laboratory environment at an average temperature of  $25 \pm 2^\circ\text{C}$ .

### Materials characterizations

$^1\text{H}$  nuclear magnetic resonance ( $^1\text{H}$  NMR) and  $^{17}\text{O}$  nuclear magnetic resonance ( $^{17}\text{O}$  NMR) were conducted on a Bruker (AVANCE III, HD 500 MHz) NMR spectrometer. The NMR spectra were calibrated to an internal capillary tube containing  $\text{D}_2\text{O}$  within NMR tube. Scanning electron microscopy (SEM, JEOL JSM-7600F) equipment was used to investigate the microstructure. Fourier transform infrared spectroscopy (FTIR) spectra were recorded using a Thermo (Nicolet 6700) system with a resolution of  $4 \text{ cm}^{-1}$ . X-ray diffraction (XRD) patterns were collected on a Bruker D8 Advanced X-ray diffractometer with  $\text{Cu K}\alpha$  radiation. X-ray photoelectron spectroscopy (XPS) tests were performed on an XPS instrument (PHI, Model 5600). The  $\text{Ar}^+$  sputtering rate was estimated to be about  $5 \text{ nm min}^{-1}$ . The high/low frequency Raman data were carried out by a Raman spectroscopy (Horiba LabRAM HR Evolution) using a laser with a wavelength of 532 nm. High-angle annular dark-field scanning transmission electron microscopy (HAADF-STEM) mode was conducted on JEM-ARM200F NeoARM with a spherical aberration corrector at 200 kV. HAADF-STEM samples were prepared using a focused ion beam (FIB) of FIB-SEM (ZEISS Crossbeam 540). The SEM, XRD, XPS, FIB-SEM, and HAADF-STEM characterizations were all conducted in an ex-situ manner of bare and post-cycling electrodes. The post-cycling electrode samples were retrieved from the cells under laboratory environment at an average temperature of  $25 \pm 2^\circ\text{C}$ . The harvested post-cycling electrodes were first rinsed thoroughly with deionized water three times to remove residual electrolyte throughout the electrode, followed by two rinses with isopropanol to eliminate remaining water. The electrodes were then dried in a vacuum oven at  $80^\circ\text{C}$  for 4 h to ensure complete removal of residual isopropanol. Finally, the dried electrodes were sealed in airtight self-sealing bags for storage and subsequent characterizations. The viscosities of different electrolytes were carried by a rolling ball viscometer (Anton Paar Lovis 2000 M).

### Electrochemical measurements

Two-electrode and three-electrode Swagelok-type configurations were supported by SCI Materials Hub (Supplementary Figs. 102, 103), where two electrodes (Zn and Zn, Cd and Cd, Zn and Cu, Cd and Cu, Cd and PANI, Cd and  $\text{V}_2\text{O}_5$ , Cd and AC, or Cd and  $\text{CdI}_2$ ) were separated by a glass fiber separator (GF/A, Whatman, one layer,  $2.7 \mu\text{m}$  particle retention,  $\sim 80\text{--}90\%$  porosity,  $675 \mu\text{m}$  thickness,  $12 \text{ mm}$  diameter) using electrolytes of about  $80 \mu\text{L}$ . The stacked scaled-up  $\text{Cd}|\text{CdI}_2$  cell was assembled using a  $100 \mu\text{m}$ -thick Cd foil as the negative electrode and a  $\text{CdI}_2$ -based cathode with sizes of  $7 \text{ cm} \times 7 \text{ cm}$  (Fig. 7a). The positive electrode was prepared with a total  $\text{CdI}_2$  material loading of  $1100 \text{ mg}$ , using a mass ratio of  $\text{CdI}_2$ : AC: KB: PTFE =  $7.5:1.5:1:0.5$ . A single layer of glass fiber separator (Whatman GF/A,  $2.7 \mu\text{m}$  particle retention,  $675 \mu\text{m}$  thickness,  $\sim 80\text{--}90\%$  porosity,  $7 \text{ cm} \times 7 \text{ cm}$  in size) was placed between the electrodes. An electrolyte volume of  $500 \mu\text{L}$  was added to the glass fiber separator using a syringe. Ti plates with tabs were used as current collectors on both the negative and positive electrode sides. PTFE plates were employed as the outer casings for both electrodes. The cell was assembled in the following sequence and secured using

screws and nuts: PTFE plate, Ti current collector, Cd negative electrode, separator,  $\text{CdI}_2$  positive electrode, Ti current collector, and PTFE plate. The stacked configuration for the scaled-up cell was supported by SCI Materials Hub. No external stack pressure was applied during battery testing. Electrochemical impedance spectroscopy (EIS) was performed in potentiostatic mode after the cells were rested for 1 h at open-circuit voltage (OCV), using a  $10 \text{ mV}$  voltage perturbation around the OCV over a frequency range of  $1 \text{ MHz}$  to  $10 \text{ mHz}$ , with 12 data points per decade and logarithmic spacing. EIS, linear sweep voltammetry (LSV), and Cyclic voltammetry (CV) profiles were collected by a Biologic VMP3 system. Charge-discharge with/without aging process tests of the  $\text{Zn}||\text{Zn}$  symmetric cells,  $\text{Cd}||\text{Cd}$  symmetric cells,  $\text{Zn}||\text{Cu}$  cells,  $\text{Cd}||\text{Cu}$  cells,  $\text{Cd}||\text{PANI}$  full cells,  $\text{Cd}||\text{AC}$  full cells,  $\text{Cd}||\text{V}_2\text{O}_5$  full cells, high-loading  $\text{Cd}||\text{PANI}$  full cells, high-loading  $\text{Cd}||\text{CdI}_2$  full cells and scaled-up  $\text{Cd}||\text{CdI}_2$  full cells, as well as the electro-deposition and electro-dissolution experiments using separator-free  $\text{Cd}||\text{Cu}$  and  $\text{Zn}||\text{Cu}$  cells (Supplementary Fig. 104) were carried out using the galvanostatic method on a multichannel Neware instrument. All the detailed electrochemical test conditions, including current density, areal capacity, load mass of electrodes, and N/P ratio, were given in the Manuscript and Supplementary Information. Unless otherwise specified, the electrochemical tests were conducted in an air-conditioned laboratory environment with an average temperature of  $25 \pm 2^\circ\text{C}$ . The specified high- and low-temperature electrochemical measurements were conducted in a temperature-controlled Neware climatic chamber (MGDW-225-40HB-208V), with an average temperature deviation of  $\pm 0.5^\circ\text{C}$ . All the electrochemical testing temperatures have been explicitly indicated in the Manuscript and Supplementary Information.

### Theoretical simulations

MD simulations were performed to visualize the solvation structures of the baseline 1C and tailored 1C6N electrolytes, informed by experimental spectroscopic evidence and theoretical derivations based on the Nernst equation. The 1C electrolyte model comprised  $40 \text{ Cd}^{2+}$  ions,  $80 \text{ Cl}^-$  ions, and  $2222 \text{ H}_2\text{O}$ , while the 1C6N model included  $40 \text{ Cd}^{2+}$ ,  $240 \text{ NH}_4^+$ ,  $320 \text{ Cl}^-$ , and  $2,222 \text{ H}_2\text{O}$ . All species were spatially distributed within the cubic simulation cells to match the intended electrolyte compositions. The MD simulations were performed using the COMPASS III force field<sup>61,62</sup>, with van der Waals interactions treated using an atom-based approach and Coulombic electrostatics handled via Ewald method with a cutoff distance of  $12.5 \text{ \AA}$ . A time step of  $1 \text{ fs}$  was employed to integrate the equations of motion throughout the simulation. Following energy minimization, each system was equilibrated for  $600 \text{ ps}$  in the NPT ensemble ( $T = 298.0 \text{ K}$ ,  $P = 1 \text{ atm}$ ) using the Nose thermostat and Berendsen barostat, allowing stabilization of thermodynamic properties. Subsequent simulations under NVT conditions were carried out for an additional  $600 \text{ ps}$  to collect trajectory data for the analysis of RDFs and coordination CNs, with configurations recorded every  $5 \text{ ps}$ .

DFT calculations were employed by the DMol3 module<sup>63</sup> to calculate the total binding energy ( $\Delta E_b$ ), successive binding energy ( $\Delta E$ ), enthalpy ( $\Delta H$ ) and Gibbs free energy ( $\Delta G$ ) of the stepwise hydration and/or ionization processes for different ion clusters, as shown in the detailed parameters of Supplementary Tables 1–32. Firstly, the generalized gradient approximation (GGA) with Perdew–Burke–Ernzerhof (PBE) exchange–correlation functional was employed to fully relax ion complex cluster<sup>64,65</sup>. The DFT-D correction was considered by Grimme method. The double-numeric quality basis sets with polarization functions were used. The iterative tolerances for energy change, force and displacements were  $1 \times 10^{-5} \text{ Ha}$ ,  $0.002 \text{ Ha \AA}^{-1}$ , and  $0.005 \text{ \AA}$ , respectively<sup>66,67</sup>. In the self-consistent field (SCF) procedure,  $10^{-6} \text{ a.u.}$  was used for the convergence standard electron density. After structure optimization, single point energy calculation was executed. Using the  $\text{Cd}(\text{H}_2\text{O})_n^{2+}$  cluster ( $n = 1\text{--}6$ ) as an example, the  $\Delta E_b$ ,  $\Delta E$ ,  $\Delta H$ , and  $\Delta G$

were calculated according to the following equation:

$$\Delta E_b = E_{\text{Cd}(\text{H}_2\text{O})_n} - E_{\text{Cd}} - nE_{\text{H}_2\text{O}} \quad (1)$$

$$\Delta E = E_{\text{Cd}(\text{H}_2\text{O})_{n-1}} + E_{\text{H}_2\text{O}} - E_{\text{Cd}(\text{H}_2\text{O})_n} \quad (2)$$

where the  $E_{\text{Cd}(\text{H}_2\text{O})_n}$ ,  $E_{\text{Cd}(\text{H}_2\text{O})_{n-1}}$ ,  $E_{\text{Cd}}$  and  $E_{\text{H}_2\text{O}}$  are the energies of  $\text{Cd}(\text{H}_2\text{O})_n^{2+}$ ,  $\text{Cd}(\text{H}_2\text{O})_{n-1}^{2+}$ ,  $\text{Cd}^{2+}$  and  $\text{H}_2\text{O}$ , respectively.

$$\Delta H = H_{\text{Cd}(\text{H}_2\text{O})_n} - H_{\text{Cd}} - nH_{\text{H}_2\text{O}} \quad (3)$$

where the  $H_{\text{Cd}(\text{H}_2\text{O})_n}$ ,  $H_{\text{Cd}}$  and  $H_{\text{H}_2\text{O}}$  are the enthalpy of  $\text{Cd}(\text{H}_2\text{O})_n^{2+}$ ,  $\text{Cd}^{2+}$  and  $\text{H}_2\text{O}$ , respectively.  $H = E_{\text{DFT}} + E_{\text{ZPE}} + E_{\text{H}}$ ,  $E_{\text{DFT}}$ ,  $E_{\text{ZPE}}$ , and  $E_{\text{H}}$  are the static calculation energy, zero-point energy, and enthalpy contribution energy.

$$\Delta G = \Delta H - \Delta(T \times S) \quad (4)$$

where  $\Delta(T \times S)$  is entropy contribution energy.  $T$  is the temperature (293.0 K) and  $S$  is the entropy.

## Data availability

The authors declare that all data supporting this work are available. The relevant datasets have been publicly deposited in the Zenodo repository<sup>68</sup> and are also available from the corresponding author upon request.

## References

- Zhu, Z. et al. Rechargeable batteries for grid scale energy storage. *Chem. Rev.* **122**, 16610–16751 (2022).
- Grey, C. P. & Tarascon, J. M. Sustainability and in situ monitoring in battery development. *Nat. Mater.* **16**, 45–56 (2017).
- Choi, J. W. & Aurbach, D. Promise and reality of post-lithium-ion batteries with high energy densities. *Nat. Rev. Mater.* **2016**, 1–16 (2016).
- Liang, Y. & Yao, Y. Designing modern aqueous batteries. *Nat. Rev. Mater.* **8**, 109–122 (2023).
- Vangapally, N. et al. Lead-acid batteries and lead-carbon hybrid systems: a review. *J. Power Sources* **579**, 233312 (2023).
- Lopes, P. P. & Stamenkovic, V. R. Past, present, and future of lead-acid batteries. *Science* **369**, 923–924 (2020).
- Liu, Y. et al. Rechargeable aqueous Zn-based energy storage devices. *Joule* **5**, 2845–2903 (2021).
- Shang, Y. & Kundu, D. A path forward for the translational development of aqueous zinc-ion batteries. *Joule* **7**, 244–250 (2023).
- Gourley, S. W. D., Brown, R., Adams, B. D. & Higgins, D. Zinc-ion batteries for stationary energy storage. *Joule* **7**, 1415–1436 (2023).
- Li, C., Jin, S., Archer, L. A. & Nazar, L. F. Toward practical aqueous zinc-ion batteries for electrochemical energy storage. *Joule* **6**, 1733–1738 (2022).
- Pu, S. D. et al. Decoupling, quantifying, and restoring aging-induced Zn-anode losses in rechargeable aqueous zinc batteries. *Joule* **7**, 366–379 (2023).
- He, Z. et al. Iron metal anode for aqueous rechargeable batteries. *Mater. Today Adv.* **11**, 100156 (2021).
- Wu, X. et al. A rechargeable battery with an iron metal anode. *Adv. Funct. Mater.* **29**, 1900911 (2019).
- Wu, X. et al. Rechargeable Iron-sulfur battery without polysulfide shuttling. *Adv. Energy Mater.* **9**, 1902422 (2019).
- Xu, Y. et al. Fe-ion bolted  $\text{VOPO}_4 \cdot 2\text{H}_2\text{O}$  as an aqueous Fe-ion battery electrode. *Adv. Mater.* **33**, 2150234 (2021).
- Chang, S., Gomez, J. F. F., Katiyar, S., Morell, G. & Wu, X. Trivalent indium metal as a high-capacity, high-efficiency, low-polarization, and long-cycling anode for aqueous batteries. *J. Am. Chem. Soc.* **145**, 24746–24754 (2023).
- Chang, S. et al. Copper foil substrate enables planar indium plating for ultrahigh-efficiency and long-lifespan aqueous trivalent metal batteries. *Adv. Funct. Mater.* **34**, 2407342 (2024).
- Chang, S. et al. A high-efficiency and long-cycling aqueous indium metal battery enabled by synergistic  $\text{In}^{3+}/\text{K}^+$  interactions. *Nanoscale* **17**, 855–863 (2025).
- Li, S. et al. Aqueous nickel-ion battery with  $\text{Na}_2\text{V}_6\text{O}_{16} \cdot 2\text{H}_2\text{O}$  nanowire as high-capacity and zero-strain host material. *Chem. Eng. J.* **413**, 127441 (2021).
- Zhang, H. et al. A high-capacity Sn metal anode for aqueous acidic batteries. *Joule* **7**, 971–985 (2023).
- Wang, J. et al. A reversible four-electron Sn metal aqueous battery. *Joule* **8**, 1–11 (2024).
- Chang, S. et al. A low-acidity chloride electrolyte enables exceptional reversibility and stability in aqueous tin metal batteries. *Angew. Chem. Int. Ed.* **64**, e202414346 (2025).
- Xu, D. et al. Highly reversible tin film anode guided via interfacial coordination effect for high energy aqueous acidic batteries. *Adv. Mater.* **36**, 2408067 (2024).
- Wu, X. et al. A four-electron sulfur electrode hosting a  $\text{Cu}^{2+}/\text{Cu}^+$  redox charge carrier. *Angew. Chem. Int. Ed.* **58**, 12640–12645 (2019).
- Liang, G. et al. Commencing an acidic battery based on a copper anode with ultrafast proton-regulated kinetics and superior dendrite-free property. *Adv. Mater.* **31**, 1905873 (2019).
- Xiong, T. et al. Bismuth ion battery – A new member in trivalent battery technology. *Energy Storage Mater.* **25**, 100–104 (2020).
- Yadav, J. K., Rani, B., Saini, P. & Dixit, A. Rechargeable iron-ion ( $\text{Fe}^{2+}/\text{Fe}^{3+}$ ) batteries: recent progress, challenges, and perspectives. *Energy Adv.* **3**, 927–944 (2024).
- Grandell, L. & Höök, M. Assessing rare metal availability challenges for solar energy technologies. *Sustainability* **7**, 11818–11837 (2015).
- Wang, M. et al. Anions regulation engineering enables a highly reversible and dendrite-free nickel-metal anode with ultrahigh capacities. *Adv. Mater.* **35**, 2305368 (2023).
- Cheng, X. et al. A novel rechargeable aqueous bismuth-air battery. *Sci. China Mater.* **66**, 4615–4621 (2023).
- Yu, Z. et al. Highly reversible tin redox chemistry for stable anode-free acidic proton battery. *Joule* **8**, 1063–1079 (2024).
- Katiyar, S. et al. Unlocking the potential of cadmium plating chemistry for low-polarization, long-cycling, and ultrahigh-efficiency aqueous metal batteries. *Energy Environ. Sci.* **17**, 4770–4779 (2024).
- Morrow, H. Cadmium and cadmium alloys. *Kirk Othmer Encycl. Chem. Technol.* **52**, 1–36 (2001).
- Schwartz, M. O. Cadmium in zinc deposits: economic geology of a polluting element. *Int. Geol. Rev.* **42**, 445–469 (2010).
- Zhang, C. et al. A  $\text{ZnCl}_2$  water-in-salt electrolyte for a reversible Zn metal anode. *Chem. Commun.* **54**, 14097–14099 (2018).
- Wu, X. et al. Reverse dual-ion battery via a  $\text{ZnCl}_2$  water-in-salt electrolyte. *J. Am. Chem. Soc.* **141**, 6338–6344 (2019).
- Suo, L. et al. “Water-in-salt” electrolyte enables high-voltage aqueous lithium-ion chemistries. *Science* **350**, 938–943 (2015).
- Jiang, H. & Ji, X. Counter-ion insertion of chloride in  $\text{Mn}_3\text{O}_4$  as cathode for dual-ion batteries: a new mechanism of electrosynthesis for reversible anion storage. *Carbon Energy* **2**, 437–442 (2020).
- Jiang, H. et al. Chloride electrolyte enabled practical zinc metal battery with a near-unity Coulombic efficiency. *Nat. Sustain.* **6**, 806–815 (2023).
- Ma, L. et al. Realizing high zinc reversibility in rechargeable batteries. *Nat. Energy* **5**, 743–749 (2020).
- Collins, K. D. Charge density-dependent strength of hydration and biological structure. *Biophys. J.* **72**, 65–76 (1997).

42. Plumridge, T. H. & Waigh, R. D. Water structure theory and some implications for drug design. *J. Pharm. Pharmacol.* **54**, 1155–1179 (2002).
43. Marcus, Y. Effect of ions on the structure of water: structure making and breaking. *Chem. Rev.* **109**, 1346–1370 (2009).
44. Bonner, O. & Charles, F. J. Effect of ions on water structure. *Infrared Phys.* **13**, 233–242 (1973).
45. Pang, Q. et al. Fast-charging aluminium–chalcogen batteries resistant to dendritic shorting. *Nature* **608**, 704–711 (2022).
46. Zhang, C. et al. The electrolyte comprising more robust water and superhalides transforms Zn-metal anode reversibly and dendrite-free. *Carbon Energy* **3**, 339–348 (2020).
47. Hoang, D. et al. Vanillin: an effective additive to improve the longevity of Zn metal anode in a 30 m ZnCl<sub>2</sub> electrolyte. *Adv. Energy Mater.* **13**, 2301712 (2023).
48. Zhang, Q. et al. Modulating electrolyte structure for ultralow temperature aqueous zinc batteries. *Nat. Commun.* **11**, 4463 (2020).
49. Yang, C. et al. All-temperature zinc batteries with high-entropy aqueous electrolyte. *Nat. Sustain.* **6**, 325–335 (2023).
50. Ji, X. A perspective of ZnCl<sub>2</sub> electrolytes: the physical and electrochemical properties. *eScience* **1**, 99–107 (2021).
51. Sui, Y. & Ji, X. Electrolyte interphases in aqueous batteries. *Angew. Chem. Int. Ed.* **63**, e202312585 (2024).
52. Saha, S., Tachikawa, N., Yoshii, K., Serizawa, N. & Katayama, Y. Electrodeposition of cadmium from Lewis basic hydrophobic room-temperature ionic liquid. *Electrochemistry* **86**, 229–234 (2018).
53. Maroni, V. A. & Hathaway, E. J. Raman spectra of the CdCl<sub>2</sub>–KCl system. *Electrochim. Acta* **15**, 1837–1840 (1970).
54. Butterworth, P. et al. Calculations of the structures, stabilities, Raman-spectra, and NMR-Spectra of CdCl<sub>n</sub>(OH<sub>2</sub>)<sub>a</sub><sup>2–n</sup>, CdBr<sub>n</sub>(OH<sub>2</sub>)<sub>a</sub><sup>2–n</sup>, and ZnCl<sub>n</sub>(OH<sub>2</sub>)<sub>a</sub><sup>2–n</sup> species in aqueous solution. *J. Phys. Chem.* **96**, 6494–6500 (1992).
55. Hao, F., Verma, A. & Mukherjee, P. P. Cationic shield mediated electrodeposition stability in metal electrodes. *J. Mater. Chem. A* **7**, 18442–18450 (2019).
56. Zheng, J. & Archer, L. A. Controlling electrochemical growth of metallic zinc electrodes: toward affordable rechargeable energy storage systems. *Sci. Adv.* **7**, eabe0219 (2021).
57. Zheng, J. et al. Spontaneous and field-induced crystallographic reorientation of metal electrodeposits at battery anodes. *Sci. Adv.* **6**, eabb1122 (2020).
58. Zampardi, G. & La Mantia, F. Open challenges and good experimental practices in the research field of aqueous Zn-ion batteries. *Nat. Commun.* **13**, 687 (2022).
59. Ji, X. L. & Nazar, L. F. Best practices for zinc metal batteries. *Nat. Sustain.* **7**, 98–99 (2024).
60. Cao, L. et al. Fluorinated interphase enables reversible aqueous zinc battery chemistries. *Nat. Nanotechnol.* **16**, 902–910 (2021).
61. Sun, H., Ren, P. & Fried, J. R. The COMPASS force field: parameterization and validation for phosphazenes. *Comput. Theor. Polym. Sci.* **8**, 229–246 (1998).
62. Sun, H. COMPASS: an ab initio force-field optimized for condensed-phase applications overview with details on alkane and benzene compounds. *J. Phys. Chem. B* **102**, 7338–7364 (1998).
63. Delley, B. From molecules to solids with the DMol<sup>3</sup> approach. *J. Chem. Phys.* **113**, 7756–7764 (2000).
64. Singh, D. J. & Ashkenazi, J. Magnetism with generalized-gradient-approximation density functionals. *Phys. Rev. B* **46**, 11570 (1992).
65. Ernzerhof, M. & Scuseria, G. E. Assessment of the Perdew–Burke–Ernzerhof exchange–correlation functional. *J. Chem. Phys.* **110**, 5029–5036 (1999).
66. Wang, K. et al. Solvation sheath regulation to induce sulfide solid-electrolyte interphase on Zn metal anode. *ACS Energy Lett.* **9**, 1000–1007 (2024).
67. Wang, R. et al. Synergetic modulation on ionic association and solvation structure by electron-withdrawing effect for aqueous zinc-ion batteries. *Proc. Natl. Acad. Sci. USA* **120**, e2221980120 (2023).
68. Cui, Y. Dataset for research of aqueous cadmium-metal battery. *Zenodo* <https://doi.org/10.5281/zenodo.15425214> (2025).

## Acknowledgements

This work was financially supported by the A\*STAR RIE2025 Manufacturing, Trade and Connectivity (MTC) Programmatic Fund (M24N6b0043) administered by A\*STAR. We would like to thank Dr. Haifang Cai (Yanan University) for his assistance with DFT and MD modeling. Thanks also go to Dr. Fang Zhang from SCI Materials Hub for providing customized Swagelok-type and stacked cell molds, and for supporting the relevant battery materials.

## Author contributions

All authors approved the final version of the manuscript. Y.-F.C. and H.Y.Y. proposed research direction and conceived idea of the work. Y.-F.C. and H.-B.S. designed and performed the experiments. Y.-F.C., H.-B.S., Q.H., X.-L.L., Y.-F.L. and B.-B.G. performed the materials characterizations and data analysis. Y.-F.C. and H.-B.S. performed the electrochemical tests. Y.-F.C. and J.-J.Y. performed the theoretical studies. Y.-F.C., Y.-H.Z. and H.Y.Y. wrote the manuscript. All authors contributed to the discussion and the manuscript preparation.

## Competing interests

The authors declare no competing interests.

## Additional information

**Supplementary information** The online version contains supplementary material available at <https://doi.org/10.1038/s41467-025-60740-2>.

**Correspondence** and requests for materials should be addressed to Hui Ying Yang.

**Peer review information** *Nature Communications* thanks the anonymous, reviewers for their contribution to the peer review of this work. A peer review file is available.

**Reprints and permissions information** is available at <http://www.nature.com/reprints>

**Publisher's note** Springer Nature remains neutral with regard to jurisdictional claims in published maps and institutional affiliations.

**Open Access** This article is licensed under a Creative Commons Attribution-NonCommercial-NoDerivatives 4.0 International License, which permits any non-commercial use, sharing, distribution and reproduction in any medium or format, as long as you give appropriate credit to the original author(s) and the source, provide a link to the Creative Commons licence, and indicate if you modified the licensed material. You do not have permission under this licence to share adapted material derived from this article or parts of it. The images or other third party material in this article are included in the article's Creative Commons licence, unless indicated otherwise in a credit line to the material. If material is not included in the article's Creative Commons licence and your intended use is not permitted by statutory regulation or exceeds the permitted use, you will need to obtain permission directly from the copyright holder. To view a copy of this licence, visit <http://creativecommons.org/licenses/by-nc-nd/4.0/>.

© The Author(s) 2025